# First-principles studies of the structural, elastic and optical properties of non-centrosymmetric cyclophosphates

© Yu.N. Zhuravlev

Kemerovo State University,
Kemerovo, Russia

E-mail: zhur@kemsu.ru

Using density functional theory methods using gradient, hybrid, short- and long-range hybrid functionals, including taking into account the dispersion correction, in the basis of localized atomic orbitals of the CRYSTAL package, calculations of the crystal and electronic structure, elastic, piezoelectric, linear and nonlinear optical properties of hexagonal $KMg(PO_3)_3$, $KCa(PO_3)_3$, $RbCd(PO_3)_3$, trigonal $KZn(PO_3)_3$, $RbZn(PO_3)_3$, tetragonal $K_2Sr(PO_3)_4$ cyclophosphates. It been shown that in hexagonal phosphates, fluorine and oxygen atoms form $[P_3O_9]$ rings, in tetragonal phosphates — $[P_4O_{12}]$, in trigonal phosphates — $[P_3O_9]$ trimers, united through zinc atoms into hexagonal rings around $K(Rb)$ atoms. Band structures and partial densities of electronic states were calculated, and the nature of valence and unoccupied states was determined. Elastic constants and moduli were calculated and conclusions were drawn about the plasticity or fragility of materials, and from the components of the piezotensor about their mechanoelectric properties. The coefficients of second harmonic generation and birefringence were obtained and the use as nonlinear optical materials was assessed.

**Keywords:** density functional theory, double phosphates, cyclophosphates, elastic modulus, IR spectra, piezoelectric coefficients, nonlinear optical properties.

## 1. Introduction

Nonlinear optical (NLO) crystals play an important role in producing coherent light in the ultraviolet (UV) and deep ultraviolet (DUV) regions with wavelengths below 200 nm. They are used as laser radiation sources in semiconductor photolithography, photochemical synthesis, medical and scientific instrumentation, and optoelectronic devices. Developing new UV-NLO materials with good second harmonic generation (SHG) characteristics and short phase-matching cutoff wavelength is an important and challenging task [1]. From the point of view of crystal structure, NLO materials used and planned for use should meet the following requirements [2]: have non-centrosymmetric (NCS) space symmetry groups; contain anions in $\pi$-delocalized systems, include transition metal cations with filled $d^{10}$ shells. From the point of view of their optical properties, the following is required [3]: a short absorption edge ($\lambda$) or a large band gap ($E_g$); large coefficients of SGH ($g_{ij}$), which should be higher than that of the standard sample of $KH_2PO_4$ (KDP), $\sim 0.39$ pm/V [4]); moderate birefringence ($\Delta n = 0.07-0.1$). Also, NLO materials should be chemically and mechanically stable and should have low cost for commercial production. There is a large number of studies, both on general issues of new NLO materials [5–8] and on their individual representatives: borates [3,9], carbonates [2,10], nitrates [11,12]. Planar and isoelectronic anions $NO_3^-$, $CO_3^{2-}$, $BO_3^{3-}$, having moderate birefringence and large second harmonic generation coef-

ficients, are considered the most favorable units for UV- and DUV-radiation. However, they also have a number of disadvantages. Carbonates decompose easily, making it difficult to grow large crystals, and nitrates tend to be hygroscopic.

Phosphates have also been considered as promising candidates for DUV-NLO materials with SHG responses of $0.1-13.5$ times greater than that of KDP and a cut-off edge in the range of $162-350$ nm ([13,14]). The phosphate group $[PO_4]^{3-}$ plays a unique and crucial role in the development and search for new NLO materials due to its wide gap between the highest occupied and the lowest unoccupied molecular orbitals, (HOMO-LUMO) of 9.6 eV and a large hyperpolarizability of 7.1 a.u. (1 a.u. = 27.21 eV). The good NLO characteristics of phosphates are explained by the diversity of aggregation and polymerization; examples are: isolated $[PO_4]^{3-}$, isolated dimer $[P_2O_7]^{4-}$, isolated trimer $[P_3O_{10}]^{5-}$, $[P_nO_{3n}]^{n-}$ ($n \leq 3$), ring and one-dimensional (1D) chain $[PO_3]_\infty$. As condensation of aggregation increases, the intensity of SHG increases according to the trend of $[P_2O_7]^{4-} < [P_3O_{10}]^{5-} < [PO_3]_\infty$, indicating that 1D chains may be beneficial for stronger SHG [15]. From a structural point of view, DUV-transparent phosphates can be divided into orthophosphates and polyphosphates [16]. Orthophosphates with $[PO_4]_n$ as anionic groups include, for example, $LiCs_2PO_4$ (2.6 KDP, $\lambda < 174$ nm) [17], $LiRb_2PO_4$ (0.6 KDP, $< 170$ nm) [18], $Rb_3Al_2(PO_4)_3$ (0.6 KDP, $< 240$ nm) [19], and orthophosphates with hexacoordinated groups include $KTiOPO_4$

(8.3 KDP, < 350 nm) [20]. In orthophosphates, the $[PO_4]^{3-}$ tetrahedra are isolated from each other, and in polyphosphates, the $PO_4$ tetrahedra are connected by common angles, forming a chain structure including dimers $[P_2O_7]^{4-}$ as in $Rb_2Ba_3(P_2O_7)_2$ (0.30 KDP, < 200 nm) [15], trimers $[P_3O_{10}]^{5-}$ as in $Ba_3P_3O_{10}Br$ (0.5 KDP, < 200 nm) [21], and infinitely condensed chains $[PO_3]_n$ as in $K_2Sr(PO_3)_4$ (0.5 KDP, < 200 nm) [16], $RbBa_2(PO_3)_5$ (1.4 KDP, < 163 nm) [15], or hexacoordinate groups as in $RbCdP_3O_9$ (0.1 KDP, < 190 nm) [22] or $LiZnP_3O_9$ (0.2 KDP, < 204 nm) [23]. Cyclophosphates with $[P_3O_9]^{3-}$ groups in the structure are known as cyclotriphosphates, and $[P_4O_{12}]^{4-}$ are known as cyclotetraphosphates.

Inorganic phosphates are one of the most popular compounds in the development of functional materials such as fluorescers, ionic conductors, ion exchangers, etc. Among them, the family of triple phosphates $M1M2(P_xO_y)$ stands out, where $M1$ is ion of an alkali metal — potassium, rubidium, and $M2$ is ion of an alkaline earth metal or a transition metal. Their crystalline framework is built by anionic groups $(P_3O_9)^{3-}$, $(P_4O_{12})^{4-}$ by connecting corners or edges. In [14], it is shown that NLO crystals assembled from non-$\pi$-conjugated tetrahedral functional structural units belonging to $[PO_4]$ usually exhibit weak nonlinearity and poor birefringence. In [24], two new DUV-NLO phosphates are reported, $KZn(PO_3)_3$ and $RbZn(PO_3)_3$, which exhibit phase matching with relatively high SHG intensity approximately 0.6 and 0.7 times larger than that of KDP, and with short cutoff edges (< 200 nm). Attraction of cations with filled $d^{10}$-shells ($Zn^{2+}$, $Cd^{2+}$) in phosphates can balance the transparency in the DUV range (i.e. extremely wide band gap) and the high intensity NLO. Calculations with the generalized gradient (GGA) exchange-correlation (XC) functional of density functional theory (DFT) in the basis of augmented plane waves show the synergy of the distorted octahedron $[ZnO_6]$ and the flexible chain $[PO_3]_\infty$, which contribute to the value of $g_{16}$, respectively, by 14 and 84% in $KZn(PO_3)_3$ or 6 and 93% in $RbZn(PO_3)_3$. Theoretical calculation by the method of pseudopotential in the basis of plane waves based on the density functional theory with gradient PBE and hybrid HSE06 functionals was also performed for $K_2SrP_4O_{12}$ [16]. The calculated band gaps for them are 5.627 and 7.35 eV, which correspond to the experimental value greater than 6 eV.

According to [16], $K_2Sr(PO_3)_4$ crystallizes in the acentric tetragonal space group $I\bar{4}$ (№ 82). The asymmetric unit consists of one unique potassium atom K, one strontium atom Sr, a phosphorus atom P, and three oxygen atoms O1, O2, O3. The P atoms coordinate with four oxygen atoms to form distorted tetrahedra of $PO_4$; the Sr atoms form polyhedra of $[SrO_8]$ with eight oxygen atoms, and potassium atoms form the polyhedron of $[KO_{10}]$. The main building groups $K_2Sr(PO_3)_4$ are rings of $[P_4O_{12}]^{4-}$ built up by four $PO_4$ corner-sharing tetrahedra. These rings are additionally connected by $[SrO_8]$ polyhedra to create a three-dimensional framework. Isostructural $KZn(PO_3)_3$ and $RbZn(PO_3)_3$ crystallize with an asymmetric space group $R3$

(№ 146) [24]. The asymmetric unit is one K (Rb) atom coordinated in the $[KO_9]/[RbO_9]$ polyhedron, one Zn atom in the $[ZnO_6]$ octahedral surrounding, one P atom and three oxygen atoms O1, O2, O3 in the $PO_4$ tetrahedron. Due to the sharing of O3 atoms, the $PO_4$ tetrahedron forms a $[PO_3]_\infty$ chain along $c$ axis, which is further connected through the distorted octahedra of $[ZnO_6]$ by the shared O1 and O2 atoms in a three-dimensional (3D) structure with $K^+/Rb^+$ cations located in the cavities.

$RbCdP_3O_9$ crystals were grown by the high-temperature melt method of [22] and belong to the space group $P\bar{6}c2$. The lattice contains a three-membered ring structure consisting of three $[PO_4]$ tetrahedra connected by a shared vertex. They form a three-dimensional framework built up by $[CdO_6]$ octahedra and rings due to the corners sharing, and charge-balanced $Rb^+$ cations are located in structural cavities. $KCa(PO_3)_3$, $KMg(PO_3)_3$ also belong to the $P\bar{6}c2$ [25,22] crystal class, but they have been less studied. $KCa(PO_3)_3$ doped with $Eu^{3+}$ ions is known for its luminescent properties [26]. $KMg(PO_3)_3$ exhibits SHG intensity 0.2 times greater than KDP [22]. This cyclophosphate has many advantages, including high chemical and thermal stability and strong optical absorption in the UV to blue wavelength range [27].

The purpose of this study is the ab initio calculation, with a wide range of functionals, of the crystal structure of non-centrosymmetric cyclophosphates, their electronic, vibrational structure, and the establishment of patterns in elastic, piezoelectric, and optical properties with an assessment of the possibility of their practical application.

## 2. Calculation method

The structure and physical properties of ternary crystalline phosphates were studied by density functional theory methods in combination with the Hartree–Fock (HF) method in the CRYSTAL17 software package [28]. Crystal orbitals were specified by linear combinations of localized Gaussian-type atomic orbitals, whose exponents and coefficients were determined from the full-electron [29] and pseudopotential [30] sets. The DFT functionals used were the exchange-correlation functionals in the generalized gradient approximation in one of the most common forms, i.e. PBE [31], and in the form adapted for solids, i.e. PBEsol [32], as well as hybrid functionals: the three-parameter B3LYP combining 20% Hartree-Fock exchange with the B3 exchange functional [33] and the LYP correlation functional [34], nonparametric PBE0 [35] with a 25% contribution from HF, and PBEsol0, where PBEsol is used instead of the PBE functional, as in the PBE0. Hybrid functionals were also used, where the amount of HF exchange depended on the distance between electrons. They are obtained by dividing the Coulomb operator into different ranges using an error function. In particular, corrected short-range functionals were used: HSE06 [36]

and HSEsol [37], as well as long-range corrected (LC) functionals: LC-wPBEsol [38] and CAM-B3LYP [39]. A wide choice of functionals is associated with taking into account the features of the crystal structure and the mechanisms of formation of chemical bonds of phosphates, where, in addition to individual ions, complexes and endless chains of ions are contained. A broader set of functionals has been used recently in [40] for the ab initio study of KDP.

For a correct description of physical and chemical properties of crystals with a complex structure, it is critical to take into account long-range London dispersion interactions, which are non-covalent in nature. Within the framework of standard DFT, these effects are not taken into account, which is due to the approximate nature of the exchange-correlation functionals, which is expressed in the incorrect asymptotic behavior of interaction potentials at large distances $(R)$, different from $\sim R^{-6}$. Methods for solving this problem can, although with some degree of convention, be divided into ab initio and semi-empirical methods. In the first case, the goal is to extend DFT based on the building up new, including nonlocal, functionals, for example, vdW-DF [41]. In the calculations of this study, dispersion interactions were taken into account using the semi-empirical method of DFT+D3 [42], where the total energy of the system has the form of $E_{\text{tot}} = E_{\text{DFT}} + E_{\text{disp}}^{\text{D3(BJ)}}$, and the dispersion correction is chosen in the form of [43].

The coupled perturbed Hartree–Fock (CPHF) method allows the CRYSTAL17 software to calculate linear and nonlinear optical properties of solid-state systems within the framework of periodic boundary conditions. Details of the original CPHF implementation can be found in [44]. Correlation effects have been included in the extension to the density functional theory in its generalized gradient approximation — the PBE, as well as in hybrid functionals such as B3LYP and PBE0 [45]. For solids, this procedure has been adapted in the form of CPHF/KS in [46,47]. The thresholds controlling the accuracy of the Coulomb and exchange series are set to 8, 8, 8, 8, 16. The reciprocal space is sampled using the $12 \times 12$ Monkhorst–Pack grid [48] with 133 independent **k**-points in the irreducible part of the Brillouin zone. The accuracy of the self-coupling procedure was no worse than $10^{-9}$ a.u.

## 3. Crystal and electronic structure

Optimization of the crystal structure, both in terms of crystal lattice constants and atomic position coordinates, is the basis for further ab initio studies of material properties. It is important to select a computational model so that it reproduces experimental crystallographic data as accurately as possible. For this purpose, functionals should be used that are capable of describing to varying degrees certain types of interactions between structural elements of crystals of double alkali-alkaline earth carbonates and the structure of butschliite, eithelite, and shortite [49]. It was shown that the structural and mechanical properties of these crystals

exhibit a linear dependence on the average radius of the cation, and different anisotropies of elastic properties under pressure are explained by the electrostatic interaction of the alkali (alkaline earth) metal ion and oxygen.

$KCa(PO_3)_3$ (hereinafter referred to as KCPO) crystallizes into a hexagonal lattice [25], in the lattice cell of which the Ca, K atoms occupy symmetrical positions $(1/3, 2/3, 0)$, $(2/3, 1/3, 0)$, P $(x_P, y_P, 3/4)$, O1 $(x_{O2}, y_{O2}, z_{O2})$, O2 $(x_{O1}, y_{O1}, 3/4)$. Atoms in $KMg(PO_3)_3$ (hereinafter referred to as KMPO) and $RbCd(PO_3)_3$ (hereinafter referred to as RCPO) have similar coordinates [22]. The distances between atoms of $M1, M2$ metals are determined by the lattice constants $a, c$, which also determine the cell volume $V$. The coordinates of oxygen atoms are manifested in the interatomic distances of $M1-O$, $M2-O$ and in $P-O$ distance between phosphorus and oxygen. Since the oxygen atoms occupy nonequivalent positions of O1 and O2, there will be a total of five nonequivalent distances. Thus, to assess the use of a particular functional, eight parameters were used, and its value was calculated as root-mean-square deviation $\Delta$ of calculated results from the experimental data. The corresponding constants, distances, and deviations for some functionals are shown in Table 1.

In the hexagonal structure of KCPO, metal atoms and anion atoms form alternating layers, and each calcium atom is surrounded by six O1 oxygen atoms at a distance of 2.324 Å (hereinafter the results of calculations with the LC-wPBEsol functional are presented, unless otherwise specified). The potassium atom is surrounded by six O1 oxygen atoms at a distance of 2.7478 Å and another six O2 atoms at a distance of 3.7221 Å. Phosphorus and oxygen atoms form a $[P_3O_9]$ ring with the P−2O1 bond length of 1.4947 Å and the P−O2 bond length of 1.6040, 1.6048 Å. Figure 1 shows the distribution of the deformation density $\Delta\rho$ obtained by subtracting the electron density of non-interacting atoms from the crystalline density. Positive areas of $\Delta\rho$ mean inflow of charge as a result of interaction, negative areas mean outflow of charge. It can be seen that the charge from the internal region of the atom inflows onto the P−O bond line and onto the Ca−O line, as well as in the region behind the oxygen nuclei. In Figure 1, calcium atoms are located above and below the plane of the ring center. In the direction of $c$ axis, these rings are combined through potassium atoms into $Z$-shaped chains.

For a calcium atom, the total population of its electron shells is $18.42e$ ($e$ being electron charge), thus, the effective charge of the calcium ion $Q_{\text{Ca}}$ is equal to $+1.58|e|$, the charge of potassium is $+0.84|e|$, and the charge of phosphate anion is $-0.807|e|$. The overlap population of electron shells of phosphorus and O1 atoms $P_{\text{P}-\text{O1}}$ is equal to $0.532e$, and for two O2 atoms it is 0.320 and $0.323e$, respectively. For isostructural KMPO: $Q_{\text{Mg}} = 1.45|e|$, $Q_{\text{K}} = 0.84|e|$, $Q_{\text{PO3}} = -0.763|e|$, for RCPO: $Q_{\text{Cd}} = 1.27|e|$, $Q_{\text{Rb}} = 0.92|e|$, $Q_{\text{PO3}} = -0.73|e|$. Thus, the covalent component of the chemical bond with the population of $P_{\text{P}-\text{O2}}$ and the ionic component with a smaller

**Table 1.** Experimental (Exp.[Ref]) and calculated with different functionals lattice constants $a, c$, volume $V$, distances between metal atoms $M1$ (K, Rb), $M2$ (Mg, Ca, Cd) and oxygen O1, O2 of hexagonal phosphates and root-mean-square deviations $\Delta$ between them

| Method | $a$, Å | $c$, Å | $V$, Å$^3$ | $M2-6$O1, Å | $M1-6$O1, Å | P$-2$O1, Å | P$-$O2, Å | P$-$O2, Å | $\Delta$, % |
|---|---|---|---|---|---|---|---|---|---|
| | | | | KCa(PO$_3$)$_3$ | | | | | |
| Exp. [25] | 6.8090 | 10.3760 | 416.61 | 2.3309 | 2.7955 | 1.4785 | 1.592 | 1.5950 | |
| PBE | 6.9203 | 10.5786 | 438.743 | 2.3563 | 2.8022 | 1.5309 | 1.6523 | 1.6543 | 3.10 |
| PBE-D3 | 6.8435 | 10.5059 | 426.113 | 2.3352 | 2.7463 | 1.5283 | 1.6482 | 1.6502 | 2.40 |
| PBE0 | 6.8538 | 10.5603 | 429.612 | 2.3466 | 2.7909 | 1.5127 | 1.6285 | 1.6292 | 1.90 |
| PBE0-D3 | 6.7736 | 10.4835 | 416.561 | 2.3249 | 2.7310 | 1.5103 | 1.6243 | 1.6255 | 1.55 |
| PBEsol | 6.8144 | 10.5432 | 423.994 | 2.3257 | 2.7503 | 1.5253 | 1.6418 | 1.6429 | 2.16 |
| PBEsol0 | 6.7728 | 10.5350 | 418.514 | 2.3231 | 2.7501 | 1.5090 | 1.6220 | 1.6221 | 1.43 |
| HSEsol | 6.7754 | 10.5323 | 418.730 | 2.3236 | 2.7507 | 1.5092 | 1.6221 | 1.6222 | 1.42 |
| LC-wPBEsol | 6.7264 | 10.5690 | 414.129 | 2.3240 | 2.7478 | 1.4947 | 1.6040 | 1.6048 | 1.14 |
| B3LYP | 6.8890 | 10.6070 | 435.947 | 2.3562 | 2.8071 | 1.5185 | 1.6375 | 1.6394 | 2.56 |
| CAM-B3LYP | 6.8099 | 10.5615 | 424.175 | 2.3373 | 2.7660 | 1.5105 | 1.6256 | 1.6270 | 1.61 |
| | | | | KMg(PO$_3$)$_3$ | | | | | |
| Exp. [22] | 6.6026 | 9.775 | 369.05 | 2.0693 | 2.7752 | 1.4762 | 1.589 | 1.592 | |
| PBE | 6.7190 | 9.9921 | 390.662 | 2.0833 | 2.8039 | 1.5292 | 1.6509 | 1.6556 | 3.31 |
| PBE-D3 | 6.6549 | 9.9128 | 380.194 | 2.0630 | 2.7563 | 1.5263 | 1.6463 | 1.6512 | 2.52 |
| PBE0 | 6.6532 | 9.9305 | 380.690 | 2.0693 | 2.7854 | 1.5110 | 1.6259 | 1.6324 | 2.00 |
| PBE0-D3 | 6.5874 | 9.8483 | 370.104 | 2.0488 | 2.7347 | 1.5083 | 1.6217 | 1.6279 | 1.45 |
| PBEsol | 6.6300 | 9.9271 | 377.905 | 2.0565 | 2.7528 | 1.5236 | 1.6395 | 1.6456 | 2.27 |
| PBEsol0 | 6.5852 | 9.8840 | 371.197 | 2.0492 | 2.7447 | 1.5072 | 1.6186 | 1.6256 | 1.42 |
| HSEsol | 6.5879 | 9.8849 | 371.536 | 2.0498 | 2.7461 | 1.5075 | 1.6189 | 1.6257 | 1.43 |
| LC-wPBEsol | 6.5448 | 9.8649 | 365.948 | 2.0450 | 2.7370 | 1.4930 | 1.6010 | 1.6082 | 1.03 |
| B3LYP | 6.6975 | 9.9727 | 387.413 | 2.0813 | 2.8058 | 1.5169 | 1.6363 | 1.6408 | 2.7 |
| CAM-B3LYP | 6.6271 | 9.9058 | 376.768 | 2.0608 | 2.7673 | 1.5087 | 1.6240 | 1.6291 | 1.65 |
| | | | | RbCd(PO$_3$)$_3$ | | | | | |
| Exp. [22] | 6.8401 | 10.176 | 412.32 | 2.261 | 2.884 | 1.467 | 1.579 | 1.601 | |
| PBE | 6.9890 | 10.4272 | 441.098 | 2.2848 | 2.9160 | 1.5311 | 1.6506 | 1.6624 | 3.81 |
| PBE-D3 | 6.9242 | 10.3538 | 429.896 | 2.2671 | 2.8642 | 1.5284 | 1.6463 | 1.6591 | 3.00 |
| PBE0 | 6.9167 | 10.4014 | 430.942 | 2.2723 | 2.9010 | 1.5123 | 1.6264 | 1.6368 | 2.52 |
| PBE0-D3 | 6.8493 | 10.3234 | 419.419 | 2.2542 | 2.8453 | 1.5098 | 1.6226 | 1.6333 | 1.84 |
| LC-wPBE-D3 | 6.8110 | 10.3126 | 414.312 | 2.2432 | 2.8307 | 1.5051 | 1.6170 | 1.6273 | 1.64 |
| PBEsol | 6.8871 | 10.3689 | 425.922 | 2.2505 | 2.8636 | 1.5254 | 1.6394 | 1.6517 | 2.65 |
| PBEsol0 | 6.8398 | 10.3537 | 419.485 | 2.2463 | 2.8586 | 1.5086 | 1.6193 | 1.6303 | 1.77 |
| HSEsol-D3 | 6.7959 | 10.2858 | 411.395 | 2.2351 | 2.8163 | 1.5071 | 1.6172 | 1.6273 | 1.75 |
| LC-wPBEsol | 6.7865 | 10.3816 | 414.087 | 2.2409 | 2.8564 | 1.4936 | 1.6023 | 1.6117 | 1.25 |
| B3LYP-D3 | 6.8441 | 10.3448 | 419.646 | 2.2563 | 2.8323 | 1.5135 | 1.6290 | 1.6408 | 2.10 |
| CAM-B3LYP | 6.8832 | 10.4150 | 427.336 | 2.2667 | 2.8832 | 1.5097 | 1.6247 | 1.6342 | 2.25 |

fraction of $P_{K-O1} = 0.13$, $P_{Rb-O1} = 0.01$ are responsible for the formation of the ring.

Let us consider the effect of the choice of DFT functionals on the results of calculating the crystallographic parameters of KCPO. Using the GGA functional in the PBE form results in a root-mean-square deviation of 3.10%. It includes a relatively low deviation of $\Delta = 0.79\%$ for $M-O$ distances and a high deviation of $\Delta = 3.69\%$ for P$-$O. Taking into account the dispersion interaction of PBE-D3 reduces the root-mean-square deviation due to lower lattice constants and P$-$O distances. The use of the hybrid functional PBE0 also overestimates the cell volume compared to the experiment, but it significantly improves the calculation of

interatomic distances of $M-O$ (0.49%) and P$-$O (2.25%). The inclusion of the dispersion correction D3(BJ) in the total energy in the PBE0-D3 method provides the most successful combination of $a, c$ parameters, so that the calculated cell volume $V$ almost perfectly coincides with the experimental one. For crystallographic parameters, the use of such a calculation scheme is better than the short-range HSE06 ($\Delta = 1.92\%$) and long-range LC-wPBE ($\Delta = 1.64\%$) functionals.

The use of the GGA version of PBEsol and the hybrid PBEsol0 modified for solid bodies and surfaces significantly improves the root-mean-square deviation in both lattice parameters and interatomic parameters. The short-range

functional HSEsol gives an equivalent result, and the long-range functional LC-wPBEsol provides the best root-mean-square deviation of 1.14%, including the best deviation of 0.85% for P−O-distances.

Another commonly used hybrid functional, B3LYP, significantly overestimates the values of both lattice constants and interatomic distances. With the dispersion correction D3, the resulted $\Delta$ is improved, but even the long-range functional CAM-B3LYP shows worse results for these cyclotriphosphates than the calculation with PBE, PBEsol.

In the KZn(PO$_3$)$_3$ phosphate (hereinafter referred to as KZPO) of low symmetry $R3$ the metals occupy symmetrical positions [24]: K $(1/6, 1/3, z_K)$, Zn $(1/6, 1/3, z_{Zn})$, and the P, O1, O2, O3 atoms are shared atoms. To determine the optimal choice of the functional, 11 non-equivalent values of crystallographic parameters were used — Table 2.

Each Zn atom in this structure is surrounded by three O1 oxygen atoms at a distance of 2.0513 Å and three more O2 atoms at 2.0635 Å, so that the octahedral environment is preserved. For the K atoms, three O1 atoms are at a distance of 2.7289 Å, three O2 atoms are at a distance of 2.8170 Å, and three more atoms are at 3.0753 Å. Here potassium is in a nine-atom surrounding. The O2 atom is slightly closer to phosphorus than O1 (in the experiment of [24] they are at the same distance), and the two O3 atoms are at a noticeably greater distance.

The distribution of the strain density of RZPO (Figure 2) in $xy$ plane, $z = 0.0002c$, where phosphorus atoms are located, indicates the formation of a bound structure of three phosphate anions [P$_3$O$_9$], united through zinc atoms with coordinates $z_{Zn} = \pm0.131c$. The three [P$_3$O$_9$] groups are combined into hexagonal rings around the $M1$ atoms with $z_K = \pm0.362c$. The overlap population on the lines of P−O1, P−O2 bonds is 0.539, 0.544$e$, respectively, and on the lines of P−O3 bonds it is 0.318, 0.303$e$. In contrast to alkaline earth metals, the population on the Zn−O1, Zn−O2 bond lines is quite high — 0.065$e$, and the effective charge of zinc is $+1.43|e|$, which is greater than that of rubidium ($+0.92|e|$). And the charge of [P$_3$O$_9$] is equal to $-2.353|e|$. In KZPO, the charge of zinc did not change, however, the charge of potassium decreased down to $+0.86|e|$.

In the tetragonal K$_2$Sr(PO$_3$)$_4$ (hereinafter referred to as KSPO), metal atoms occupy symmetrical positions [16]: K $(0, 0, z_K)$, Sr $(1/2, 0, 1/4)$, P and oxygen atoms O1, O2, O3 are shared atoms, so there will be 19 atoms in a lattice cell. Interatomic distances obtained using different functionals are listed in Table 3. The smallest root-mean-square deviations from the data of [16] (the situation with the data of [50] is similar) were shown by the long-range functional CAM-B3LYP, and with the LC-wPBEsol only the third top result was obtained.

The potassium atom is surrounded by five pairs of oxygen atoms, so this can be thought of as a polyhedron of KO$_{10}$. Strontium is surrounded by four O2 oxygen atoms at a distance of 2.4799 Å and four O1 atoms at a distance of 2.6653 Å. O3 atoms are not involved in the formation of the polyhedron of SrO$_8$. The overlap population on the
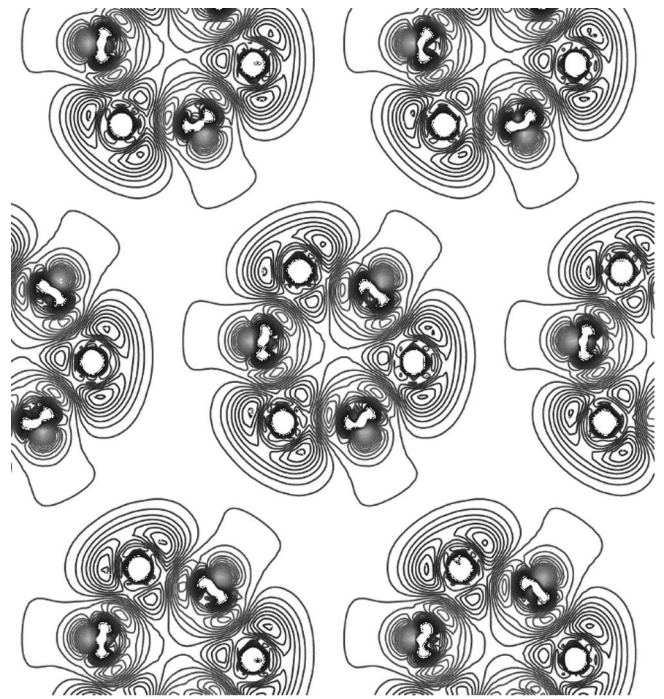


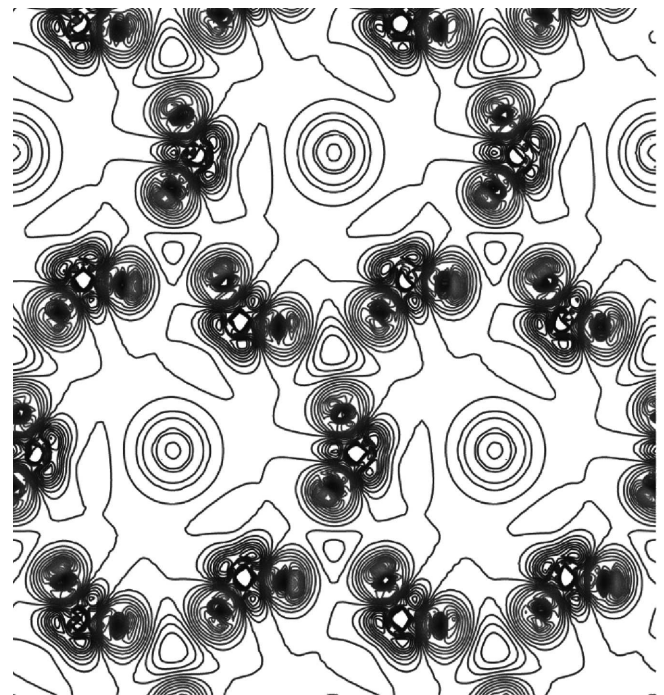**Figure 1.** Strain density distribution in the O2−P−O2 KCa(PO$_3$)$_3$ plane.



**Figure 2.** Strain density distribution in the RbZn(PO$_3$)$_3$.

Sr−O2, Sr−O1 bond line is 0.029 and 0.026$e$, which is two times greater than that of K−O. The four anions form the ring of [P$_4$O$_{12}$]. The overlap population of electron shells of the P−O1 and P−O2 atoms is 0.561, 0.526$e$, which is

**Table 2.** Experimental (Exp. [Ref]) and calculated with different functionals lattice constants $a$, $c$, volume $V$, distances between metal atoms $M1$ (K, Rb), Zn and oxygen O1, O2, O3 (all values are in Å), phosphorus and oxygen P−O (all values are in Å) of trigonal phosphates and root-mean-square deviations $\Delta$ between them

| Method | $a$, Å | $c$, Å | $V$, Å$^3$ | Zn−3O1 Zn−3O2 | $M1$−3O1 $M1$−3O2 | $M1$−3O3 | P−O1 P−O2 | P−O3 | $\Delta$, % |
|---|---|---|---|---|---|---|---|---|---|
| KZn(PO$_3$)$_3$ | | | | | | | | | |
| Exp. [24] | 10.1766 | 6.9742 | 625.50 | 2.082 2.084 | 2.767 2.857 | 3.122 | 1.481 1.481 | 1.596 1.614 | |
| PBE-D3 | 10.1972 | 6.9607 | 626.831 | 2.0803 2.0905 | 2.7195 2.8339 | 3.0477 | 1.5276 1.5296 | 1.6521 1.6777 | 2.20 |
| PBE0 | 10.2529 | 7.0066 | 637.871 | 2.0821 2.0889 | 2.7665 2.8628 | 3.1043 | 1.5119 1.5121 | 1.6305 1.6500 | 1.40 |
| PBE0-D3 | 10.1297 | 6.8971 | 612.909 | 2.0660 2.0786 | 2.7037 2.8079 | 3.0501 | 1.5093 1.5106 | 1.6273 1.6492 | 1.73 |
| PBEsol | 10.1792 | 6.9509 | 623.748 | 2.0640 2.0705 | 2.7249 2.8326 | 3.0402 | 1.5249 1.5259 | 1.6447 1.6683 | 2.04 |
| PBEsol0 | 10.1526 | 6.9222 | 617.924 | 2.0595 2.0673 | 2.7257 2.8229 | 3.0599 | 1.5083 1.5086 | 1.6234 1.6435 | 1.43 |
| HSEsol-D3 | 10.0629 | 6.8401 | 599.845 | 2.0484 2.0616 | 2.6791 2.7809 | 3.0222 | 1.5066 1.5078 | 1.6212 1.6435 | 2.33 |
| LC-wPBEsol | 10.1253 | 6.8928 | 611.979 | 2.0513 2.0635 | 2.7289 2.8170 | 3.0753 | 1.4935 1.4938 | 1.6040 1.6227 | 1.21 |
| RbZn(PO$_3$)$_3$ | | | | | | | | | |
| Exp. [24] | 10.2440 | 7.1431 | 649.2 | 2.076 2.093 | 2.871 2.925 | 3.193 | 1.469 1.475 | 1.606 1.609 | |
| PBE-D3 | 10.2906 | 7.1903 | 659.422 | 2.0791 2.0896 | 2.8447 2.9333 | 3.1046 | 1.5257 1.5286 | 1.6592 1.6785 | 2.42 |
| PBE0 | 10.3381 | 7.2184 | 668.125 | 2.0820 2.0883 | 2.8889 2.9517 | 3.1789 | 1.5103 1.5111 | 1.6362 1.6505 | 1.74 |
| PBE0-D3 | 10.2208 | 7.1128 | 643.485 | 2.0654 2.0777 | 2.8224 2.9026 | 3.1069 | 1.5075 1.5096 | 1.6334 1.6500 | 1.70 |
| PBEsol | 10.2720 | 7.1813 | 656.223 | 2.0629 2.0700 | 2.8540 2.9289 | 3.1035 | 1.5231 1.5248 | 1.6509 1.6687 | 2.21 |
| PBEsol0 | 10.2414 | 7.1368 | 648.266 | 2.0589 2.0671 | 2.8480 2.9134 | 3.1251 | 1.5066 1.5076 | 1.6288 1.6440 | 1.48 |
| HSEsol-D3 | 10.1537 | 7.0556 | 629.961 | 2.0482 2.0603 | 2.7960 2.8762 | 3.0740 | 1.5047 1.5068 | 1.6272 1.6442 | 2.17 |
| LC-wPBEsol | 10.2138 | 7.1024 | 641.669 | 2.0513 2.0630 | 2.8503 2.9053 | 3.1440 | 1.4921 1.4925 | 1.6092 1.6229 | 1.06 |

greater than that on the P−O3 line with its 0.307, 0.315$e$. The charge obtained according to the Mulliken scheme for potassium and strontium cations is equal to $+0.83|e|$ $|e|$, $+1.54|e|$ and for each phosphate anion it is $0.8|e|$.

The peculiarities of the formation of a chemical bond are manifested in the electronic properties of phosphates. Figure 3 shows a fragment of the band structure $E_n(\mathbf{k})$ and the partial density of electronic states $N(E)$ in the energy interval of $-0.25 < E < 0.35$ a.u., KCPO. The points of the Brillouin zone correspond to the coordinates of $\Gamma\,(0, 0, 0)$, M $(1/2, 0, 0)$, L $(1/2, 0, 1/2)$, A $(0, 0, 1/2)$, K $(1/3, 1/3, 0)$, H $(1/3, 1/3, 1/2)$ in units of reciprocal lattice vectors.

The difference between the energetic electronic structure of phosphates is the presence of narrow allowed energy regions and wide band gaps. Occupied (valence) bands are relatively flat, in contrast to dispersed unoccupied bands (conduction bands). The uppermost valence region (UVB) consists of six energy bands with a width of 0.48 eV, which in the density of states corresponds to a narrow band with a maximum at $-0.31$ eV. 82% of its formation is contributed by $p$-states of O1 oxygen atoms and 16% is from O2 atoms. The oxygen nature of the upper valence band is a distinctive feature of alkali-alkaline earth oxyanionic crystals [51]. The top of the valence band is realized at the K point of the Brillouin zone, and the bottom of the conduction band at its center — the $\Gamma$ point, so that the band gap $(E_g)$ is equal to 6.29 eV. The conduction band also has a feature, which consists in the presence of a discontinuity in the spectrum of unoccupied states with a width of 0.83 eV,

**Table 3.** Experimental (Exp. [Ref]) and calculated with different functionals lattice constants $a$, $c$, volume $V$, distances between atoms of K, Sr and oxygen O1, O2, O3 (all values are in Å), phosphorus and oxygen P−O (values are in Å) in $K_2Sr(PO_3)_4$ and root-mean-square deviations $\Delta$ between them

| Method | $a$, Å | $c$, Å | $V$, Å$^3$ | Sr−4O2 Sr−4O1 | K−2O1 | K−2O2 | K−2O3 | P−O1 P−O2 | P−O3 | $\Delta$, % |
|---|---|---|---|---|---|---|---|---|---|---|
| Exp. [16] | 7.446 | 10.156 | 563.1 | 2.508 2.696 | 2.786 3.273 | 2.848 2.997 | 3.055 | 1.482 1.483 | 1.612 1.618 | |
| Exp. [50] | 7.429 | 10.149 | 560.1 | 2.503 2.693 | 2.780 3.269 | 2.846 2.985 | 3.055 | 1.478 1.481 | 1.609 1.612 | |
| PBE-D3 | 7.4042 | 10.1358 | 555.684 | 2.5013 2.6870 | 2.7781 3.1905 | 2.7811 2.9716 | 3.0298 | 1.5254 1.5317 | 1.6662 1.6702 | 2.02 |
| PBESOL | 7.4027 | 10.1124 | 554.160 | 2.4838 2.6683 | 2.7724 3.2190 | 2.7890 2.9655 | 2.9996 | 1.5222 1.5280 | 1.6575 1.6637 | 1.88 |
| PBESOL0 | 7.3669 | 10.0965 | 547.958 | 2.4806 2.6650 | 2.7611 3.2102 | 2.7840 2.9586 | 3.0150 | 1.5053 1.5113 | 1.6353 1.6405 | 1.57 |
| HSEsol-D3 | 7.2578 | 9.9850 | 525.964 | 2.4635 2.6436 | 2.7194 3.1181 | 2.7269 2.9119 | 3.0082 | 1.5044 1.5100 | 1.6337 1.6372 | 2.99 |
| LC-wPBEsol | 7.3229 | 10.0757 | 540.306 | 2.4799 2.6653 | 2.7468 3.1829 | 2.7735 2.9455 | 3.0414 | 1.4904 1.4966 | 1.6158 1.6158 | 1.75 |
| CAM-B3LYP | 7.4245 | 10.1883 | 561.610 | 2.5064 2.6984 | 2.7723 3.2338 | 2.8141 2.9788 | 3.0639 | 1.5063 1.5128 | 1.6400 1.6439 | 1.08 |
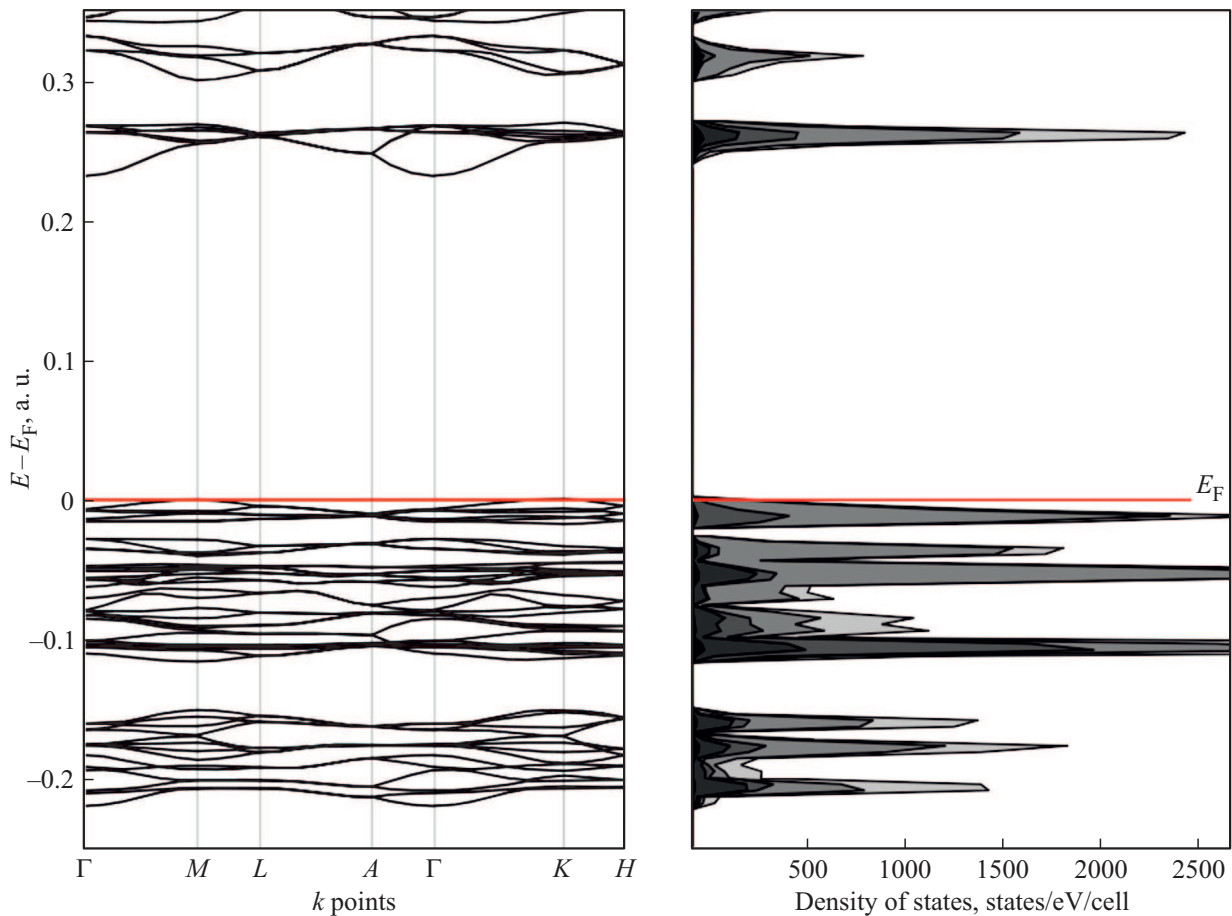


**Figure 3.** Band structure $E(\mathbf{k})$ and density of electronic states in $KCa(PO_3)_3$. The Fermi energy $E_F$ is taken as the zero energy.
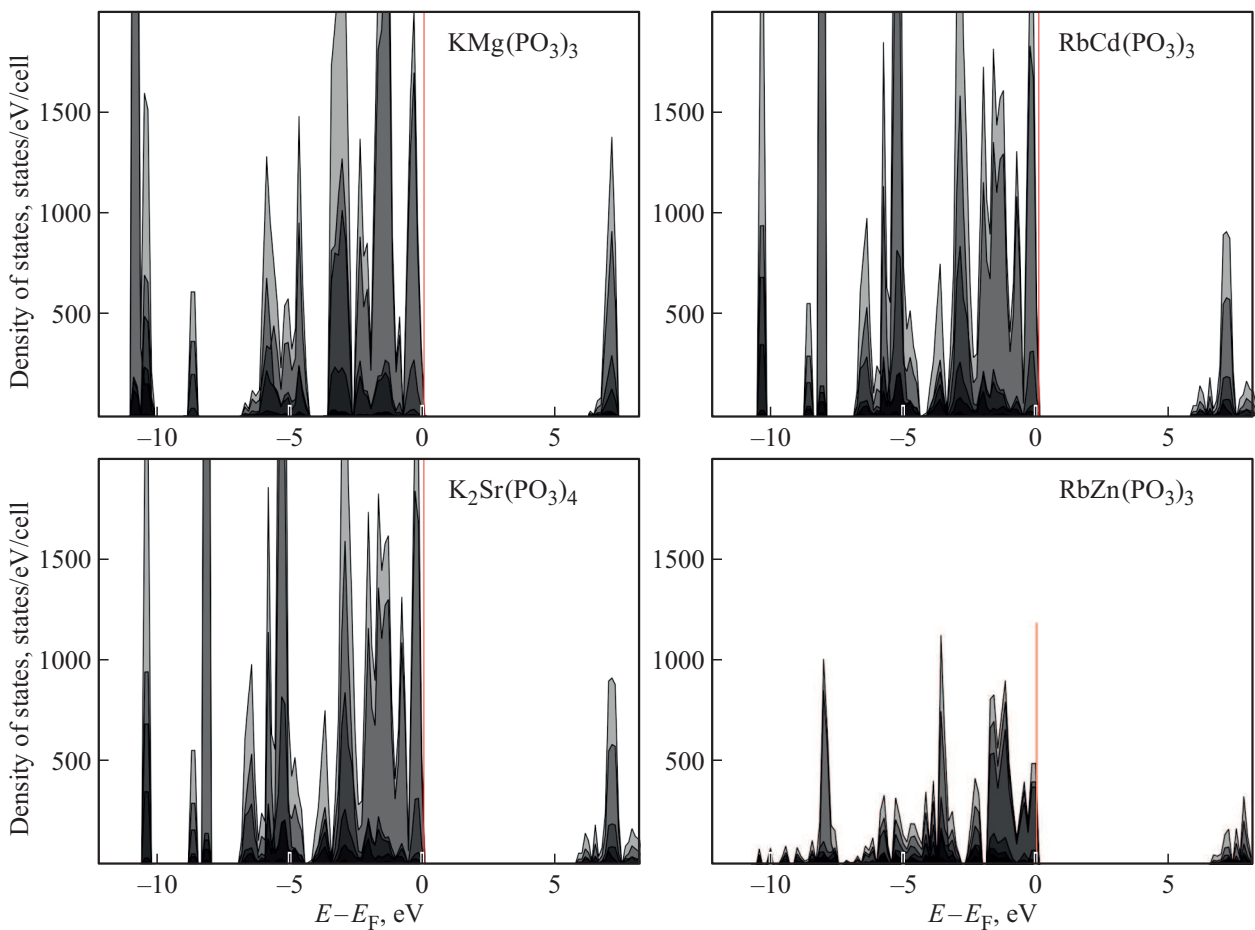
**Figure 4.** Density of electronic states in KMg(PO₃)₃, RbCd(PO₃)₃, K₂Sr(PO₃)₄, RbZn(PO₃)₃. The Fermi energy $E_F$ is taken as the zero energy.

which separates the lower conduction band (LCB) from subsequent ones. In the density of states, it corresponds to a maximum at 7.16 eV. The dominant contribution to its formation is made by $p$-phosphorus states, and the percentage of metals does not exceed 1%. The use of other functionals does not change the qualitative structure of the energy spectrum. The band gap increases for hybrid functionals as the HF exchange contribution increases: PBE0 9.39, PBEsol0 9.50, HSEsol 8.72, CAM-B3LYP 11.94 and LC-wPBEsol 16.77 eV.

The energy structure of KMPO is qualitatively similar to that in Figure 3 but with lower band widths of UVB — 0.76 eV, Eg — 5.98 eV, and LCB — 1.32 eV. Having the same structure, the RCPO (Figure 4) contains cadmium with a completely filled electron shell $4d^{10}$. $d$-states of cadmium participate in the formation of states of the upper valence regions, therefore their width is greater than those in KCPO and KMPO. Thus, the energy distance between UVB and the lower valence bands is only 0.09 eV, and its width is 0.59 eV. It is also formed from $p$-states of O1, O2, but the proportion of cadmium increases to 3%. The bands of $d$-states of cadmium are located in the region from −11.2 to −10.3 eV. The top of the valence band is realized at

the M point, and the bottom of the unoccupied band is still at Γ, and the width of the indirect band gap decreases down to 5.60 eV (8.80 PBESOL0, 8.15 HSEsol-D3, B3LYP-D3). The bunch of six isolated lower unoccupied bans has a width of 1.68 eV, and in the density of states it corresponds to a maximum at 6.83 eV. The lowest unoccupied band is formed by 45% of $s$-states of fluorine, 29% of $s$-cadmium and 19% of $p$-O2.

The band structures and densities of states of KZPO and RZPO were calculated earlier in [24]. The band gap values obtained there were 5.12 and 5.09 eV. In the KZPO, the top of the valence band is realized at the M point, and the bottom of the conduction band is at Γ, and the band gap with the PBEsol functional is 6.45 eV (9.60 eV PBE0, 9.78 eV PBEsol0, 9.11 eV HSEsol). In the RZPO, the $E_g$ is equal to 6.42 eV. In this compound, the two upper valence bands are formed by 40%, 37% of $p$-states of O1, O2 oxygen, only 1% of O3 and 14% of $d$-zinc. $s$-states of Zn are amounted to 16% of those involved in the formation of the lower unoccupied state, together with 53% of $s$-phosphorus and 14% of O3 oxygen. In the tetragonal KSPO, the upper valence bands are planar. The top of the valence band falls on the line of the Brillouin zone, and

**Table 4.** Density $\rho$ and elastic constants $C_{ij}$ (GPa) of cyclophosphates

| Crystal | $\rho$, g/cm$^3$ | $C_{11}$ | $C_{12}$ | $C_{13}$ | $C_{33}$ | $C_{44}$ | $C_{66}$ | $C_{14}$ | $C_{15}$ | $C_{16}$ |
|---------|------|------|------|------|------|------|------|------|------|------|
| KMg(PO$_3$)$_3$ | 2.635 | 121.30 | 35.61 | 44.64 | 121.92 | 32.58 | 42.84 | | | |
| KCa(PO$_3$)$_3$ | 2.474 | 77.51 | 36.63 | 43.17 | 78.40 | 7.26 | 20.44 | | | |
| RbCd(PO$_3$)$_3$ | 3.397 | 88.26 | 40.52 | 48.84 | 85.75 | 9.25 | 23.87 | | | |
| KZn(PO$_3$)$_3$ | 2.714 | 85.49 | 32.42 | 8.35 | 78.89 | 33.46 | 26.54 | 2.86 | −1.03 | |
| RbZn(PO$_3$)$_3$ | 2.928 | 82.22 | 32.96 | 7.75 | 73.55 | 34.66 | 24.63 | 2.05 | −2.59 | |
| K$_2$Sr(PO$_3$)$_4$ | 2.887 | 68.11 | 6.92 | 16.64 | 72.36 | 24.53 | 23.04 | | | −2.28 |
| KH$_2$PO$_4$ [54] | 2.338 | 71.2 | −5 | 14.1 | 56.8 | 12.6 | 6.22 | | | |

the bottom of the unoccupied band is at the $\Gamma$ $(0, 0, 0)$ point, so the width of the indirect gap will be 6.90 eV, and that of the direct gap will be 0.001 eV less. For the PBEsol0 functional this value is 10.04 eV, for the HSEsol it is 9.36 eV. According to [16], in the KSPO the width of $E_g$ for the GGA and HSE06 functionals is 5.627, 7.35 eV. The contribution of oxygen atoms to the formation of the upper bunch of eight isolated energy bands with a width of 0.51 eV and a maximum of $N(E)$ at −0.27 eV is 46% for O1, 37% for O2, 13% for O3. The three lower conduction bands with a width of 1.12 eV are separated from the subsequent ones by a band gap of 0.26 eV. The contribution of $s$-states of strontium to their formation does not exceed 3%, that for potassium is not more than 5%, and the main contribution of 60% is made by $p_z$-orbitals of phosphorus. Thus, the minimum interband transition is anionic in nature.

Metallic states form narrow $\Delta E$ and intense bands with a pronounced maximum $E_{max}$ in the valence region. Their positions in the KSPO are characterized for $p$-Sr by energies of $\Delta E = 0.2$ eV and $E_{max} = -13.3$ eV, and for $p$-K by energies of 0.3 and −10.4 eV, respectively. Their energy positions change little from compound to compound. So, for the $p$-potassium in the KZPO they are 0.3 and −10.5 eV, in the KCPO they are 0.13 and −10.6 eV, in the KMPO they are 0.19 and −10.7 eV. They can be used as reference points in the photoelectron spectra interpretation.

## 4. Elastic and piezoelectric properties

Crystalline NLO materials should offer mechanical stability, hardness, non-bleeding, ease of processing, etc. Therefore, when developing new materials, it is necessary to study their elastic properties: the factor of static mechanical stability, vibrational spectra as a factor of dynamic stability. A prerequisite for the existence of piezoelectricity is the presence of a non-centrosymmetric group in the object. All studied phosphates meet this requirement, so it is of interest to study their quantitative piezoelectric characteristics to assess their possible use.

The relationship between the second-rank stress tensor $\sigma$ and the second-rank strain tensor $\eta$ is given by the generalized Hooke's law: $\sigma_{ij} = C_{ijkl}\eta_{kl}$, $\eta_{ij} = S_{ijkl}\sigma_{kl}$, where $C_{ijkl}$ and $S_{ijkl}$ are components of the elasticity tensor $\mathbf{C}$ and compliance tensor $\mathbf{S} = \mathbf{C}^{-1}$ of the fourth rank. The $i, j, k$

and $l$ subscripts define the Cartesian directions $x, y$ and $z$. Using the Voigt notation, pairs of Cartesian indices can be represented by a single index $1 = xx$, $2 = yy$, $3 = zz$, $4 = yz$, $5 = xz$, and $6 = xy$, so instead of four only two can be used: $v, u = 1, \ldots, 6$. In this notation, the elasticity tensor $\mathbf{C}$ is represented by a symmetric $6 \times 6$ matrix. For a crystal lattice, the components of the elasticity matrix are defined as

$$C_{vu} = \frac{1}{V} \frac{\partial^2 E_{tot}}{\partial \eta_v \partial \eta_u},$$

where $E_{tot}$ being total energy. This relationship shows the equivalence of the $C_{vu}$ and $C_{uv}$ elements, which leads to the symmetry of the $\mathbf{C}$ and $\mathbf{S}$ matrices and the reduction of the number of independent components down to 21. Taking into account the symmetry of a specific crystal lattice makes it possible to further significantly reduce the number of independent constants. In hexagonal crystals there will be 5 independent components, in tetragonal crystals there will be 6 independent components, trigonal crystals will have 7 independent components. The values of elastic constants of phosphates calculated with the PBEsol functional using the algorithm of [52,53] are given in Table 4. Due to the lack of experimental data for these phosphates, measurements of [54] for KDP are given for comparison.

The elastic properties of a hexagonal crystal in the $(xy)$ layer plane are isotropic and are described by elastic constants $C_{11}$ and $C_{12}$, which characterize Young's modulus and Poisson's ratio. In all crystals $C_{12}$ have similar values, with the exception of KSPO. The $C_{33}$ constant determines the Young's modulus in the perpendicular direction. The $C_{44}$ constant describes the stress when the layers shift relative to each other. It has the lowest values in KCPO, RCPO.

There are relationships between the elastic constants that follow from the need to fulfill the stability criterion of the crystal lattice and are formulated in the book of Born [55]: the elastic constant matrix $C$ is positive definite; all eigenvalues of $C$ are positive; all leading principal minors of the $C$ matrix are positive; an arbitrary set of $C$ minors is positive. The following four necessary and sufficient conditions for elastic stability in a hexagonal (tetragonal) crystal can be derived directly calculating the eigenvalues of the stiffness matrix $C$ [56]: $C_{44} > 0$, $C_{11} > |C_{12}|$, $(C_{11} + C_{12})C_{33} > 2C_{13}^2$. Another condition, $C_{33} > C_{13}$, was derived in [57] from the conservation law. In trigonal

**Table 5.** Linear uniaxial compression moduli $B_a$, $B_c$, Young's moduli $E_a$, $E_c$ along $a$, $c$ axes (all values are in GPa)

| Crystal | $B_a$ | $B_c$ | $E_a$ | $E_c$ |
|---|---|---|---|---|
| KMg(PO$_3$)$_3$ | 196.0 | 223.9 | 101.4 | 96.5 |
| KCa(PO$_3$)$_3$ | 148.2 | 187.8 | 50.7 | 45.7 |
| RbCd(PO$_3$)$_3$ | 169.9 | 201.7 | 57.8 | 48.7 |
| KZn(PO$_3$)$_3$ | 129.9 | 90.5 | 72.3 | 77.7 |
| RbZn(PO$_3$)$_3$ | 126.9 | 83.8 | 68.1 | 72.5 |
| K$_2$Sr(PO$_3$)$_4$ | 87.5 | 116.8 | 63.9 | 65.0 |

crystals, the condition of $C_{14}^2 + C_{15}^2 > C_{44}C_{66}$ is added. It follows from Table 4 that for all cyclophosphates the conditions of mechanical stability are met.

The Cauchy pressure can be determined through elastic constants. The Cauchy pressure of a crystal is expressed as the difference between two given elastic constants $P_a = C_{13} - C_{44}$, $P_c = C_{12} - C_{66}$ [58]. The higher is the Cauchy pressure, the higher is the impact strength of the material. If the Cauchy pressure is positive, the material exhibits plastic behavior; otherwise the material exhibits brittle behavior. KCPO and RCPO exhibit plastic behavior.

Elastic properties are usually characterized by elastic moduli. Among them, the bulk modulus of elasticity $B$ characterizes the ability of a crystal to change its volume under the uniform normal stress, identical in all directions. The shear modulus $G$ characterizes the ability of a material to resist changing in shape while maintaining its volume; it is defined as the ratio of shear stress to shear strain. The Young's modulus $E$ characterizes the resistance of a material to tension/compression during elastic deformation, or the property of an object to deform along an axis when exposed to a force acting along this axis. The Poisson's ratio $\mu$ is the ratio of relative transverse compression to relative longitudinal tension.

Most crystals have elastic anisotropy, i.e. directional dependence of physical properties. The linear modulus of uniaxial compression in the directions of $a$ and $c$ is defined as $B_a = (S_{11} + S_{12} + S_{13})^{-1}$, $B_c = (S_{31} + S_{32} + S_{33})^{-1}$, the Young's modulus is $E_a = S_{11}^{-1}$, $E_c = S_{33}^{-1}$. The corresponding values are given in Table 5. Compressibility (the reciprocal of the modulus) will be less along the $c$ axis for all crystals except trigonal ones. Young's moduli have similar values for both directions.

The mechanical properties of polycrystalline materials are studied on the basis of two extreme approximations of Voigt (V) [59] and Reuss (R) [60] based on the difference between the upper and lower bounds of the bulk modulus and the shear modulus. Voigt assumes that the elasticity matrix $C_V = \langle C \rangle$ is averaged, and according to Reuss the compliance matrix $S_R = \langle S \rangle$ is averaged. When the crystallites within the aggregate are isotropic, the boundaries converge. Hill (H) [61] suggested the use of average values of $B_H = (B_V + B_R)/2$, $G_H = (G_V + G_R)/2$ as moduli, which are in better agreement with the experiment. Then

the Young's modulus and the Poisson's ratio can be obtained using the following formula: $E_H = 9B_H G_H / (3B_H + G_H)$, $\mu = (3B_H - 2G_H)/(6B_H + 2G_H)$. This data is shown in Table 6. The KZPO, RCPO, KSPO have relatively high compressibility, comparable to the KDP (35.6 GPa). The comparatively low compressibility in the KMPO is, however, less than in metal carbonates [51], double carbonates [62], and fluorocarbonates [63].

The ratio of bulk modulus to shear modulus is used to evaluate the impact strength/brittleness of materials [64]. If the value of $B_H/G_H$ is high, the strength of the material is good. If it is greater than 1.75, then the material exhibits plasticity; otherwise it exhibits brittleness. For brittle materials, the Poisson's ratio is $\mu < 0.26$, for plastic materials it is higher than 0.26. A consequence of brittleness is the sensitivity to thermal shock because the material cannot effectively dissipate thermal stresses through plastic deformation. Brittle materials are KZPO, RCPO, KSPO. Similar relationships have been established in [65] for phosphates with the structure $\beta$-quartz: $\beta$-AlPO$_4$ 2.62 and $\beta$-GaPO$_4$ 3.34 with $\mu$ values of 0.33, 0.36, respectively. Care must be taken when using brittle materials as NLO, because heat build-up is inevitable during laser operation.

The Debye temperature is a physical constant of a substance that characterizes many properties of crystals: heat capacity, electrical conductivity, thermal conductivity, etc. It can be calculated through the average velocity of elastic wave $v_{av}$ [66]:

$$\Theta_D = \frac{h}{k_B} \left( 3 \frac{N}{4\pi} N_A \frac{\rho}{M} \right)^{1/3} v_{av},$$

where $h$ is Planck's constant, $k_B$ is Boltzmann's constant, $N_A$ is Avogadro's number, $N$ and $M$ are the number of atoms in the formula unit and its molecular weight, $\rho$ is density. Low Debye temperature is demonstrated by RCPO, KSPO, KCPO, where it is less than room temperature. For others, it is higher and comparable to the data of [67] for KDP, where at 0 K $\Theta_D$ is 380 K and according to [40] it is 340 K.

In [68], recommendations have been developed for the selection of materials that can withstand high temperatures. Using existing theories of minimum thermal conductivity, the parameter $k_{min}$ (calculated minimum thermal conductivity of the lattice) is determined, which can be used to determine possible alternatives for high temperature applications. $k_{min}$ of double phosphates is given in Table 6.

For comparison, these values are 1.20 W(m·K)$^{-1}$ for $\beta$-AlPO$_4$ and 0.88 W(m·K)$^{-1}$ for $\beta$-GaPO$_4$ [65].

The origin of the low thermal conductivity in the studied phosphates is associated with the heterogeneous binding strength of atoms. Indeed, the Mulliken populations of the M−O and P−O bonds are significantly different: the P−O bonds are stronger than the M−O bonds. Strong P−O bonds can transport phonons efficiently, but transport in weaker M−O bonds is relatively slower. In addition, the crystalline framework, due to the inhomogeneous bond strength, will increase the scattering of phonons, which

**Table 6.** Bulk modulus $B_H$, shear modulus $G_H$ and Young's modulus $E_H$ (all values are in GPa), Poisson's ratio $\mu$, Debye temperature $\Theta_D$ and minimum lattice thermal conductivity $k_{min}$ for polycrystalline cyclophosphates

| Crystal | $B_H$ | $G_H$ | $E$ | $\mu$ | $\Theta_D$, K | $k_{min}$, W(m·K)$^{-1}$ |
|---|---|---|---|---|---|---|
| KMg(PO$_3$)$_3$ | 68.2 | 37.3 | 94.6 | 0.269 | 394.6 | 0.58 |
| KCa(PO$_3$)$_3$ | 53.2 | 12.9 | 35.9 | 0.388 | 234.4 | 0.33 |
| RbCd(PO$_3$)$_3$ | 59.8 | 15.4 | 42.5 | 0.382 | 217.6 | 0.31 |
| KZn(PO$_3$)$_3$ | 38.2 | 31.5 | 74.1 | 0.177 | 342.5 | 0.49 |
| RbZn(PO$_3$)$_3$ | 36.7 | 30.6 | 30.6 | 0.173 | 319.8 | 0.45 |
| K$_2$Sr(PO$_3$)$_4$ | 32.0 | 25.5 | 60.4 | 0.185 | 271.7 | 0.35 |

**Table 7.** Electromechanical coupling constants kij of cyclophosphates

| Crystal | $k_{11}, k_{22}$ | $k_{31}, k_{33}$ | $k_{26}, k_{16}$ | $k_{14}, k_{15}$ | $k_{36}$ |
|---|---|---|---|---|---|
| KMg(PO$_3$)$_3$ | 0.10 | | 0.12 | | |
| KCa(PO$_3$)$_3$ | 0.05 | | 0.07 | | |
| RbCd(PO$_3$)$_3$ | 0.03 | | 0.04 | | |
| KZn(PO$_3$)$_3$ | 0.10, 0.06 | 0.04, 0.00 | 0.12, 0.07 | 0.11, 0.08 | |
| RbZn(PO$_3$)$_3$ | 0.10, 0.07 | 0.03, 0.03 | 0.12, 0.12 | 0.10, 0.07 | |
| K$_2$Sr(PO$_3$)$_4$ | | 0.01 | | 0.21, 0.23 | 0.11 |

will also ultimately contribute to a decrease in the thermal conductivity of the lattice.

The mathematical description of piezoelectricity relates the strain (or stress) to the electric field through a third-order tensor. This tensor describes the response of any bulk piezoelectric material to an applied electric field or mechanical load. In the linear approximation, the direct and inverse piezoelectric tensors **e** and **d** describe the polarization $\eta$, and the deformation induced by an external electric field **E**. Piezoelectric constants can be calculated in Voigt notation as

$$e_{ij} = \frac{\partial P}{\partial \eta_j}\Big|_E = -\frac{\partial \sigma_j}{\partial E_i}\Big|_\eta \text{ [69]}.$$

There is a simple direct relationship between piezoelectric tensors: **e** = **d** · **C**, **d** = **e** · **S**.

In hexagonal phosphates, non-zero components $e_{11}$ in the KCPO, KMPO, RCPO series are equal to 0.075, 0.065, 0.025 C/m$^2$. In the tetragonal KSPO, the non-zero components are $e_{31} = 0.021$ C/m$^2$, $e_{14} = 0.149$ C/m$^2$, $e_{15} = 0.164$ C/m$^2$ and $E_{36} = 0.076$ C/m$^2$. In the KZPO (RCPO) non-zero components are $e_{11} = 0.094\,(0.092)$ C/m$^2$, $e_{12} = 0.051\,(0.0182)$ C/m$^2$, $e_{31} = 0.076\,(0.0612)$ C/m$^2$. To compare the values, in the lead zirconate titanate (PZT), which is well-known piezoelectric material for energy storage, the $e_{31}$ component is equal to 0.739 C/m$^2$. The components of the inverse piezotensor $d_{31} = d_{32}$ in KZPO, RZPO, KSPO are equal to 0.644, 0.518, 0.222 pm/V, respectively. For comparison: in the PZT it is 140 pm/V; in GaPO$_4$ [70] $d_{11} = 4.5$ pm/V,

$d_{14} = 1.9$ pm/V, and in quartz [71] $d_{11} = 2.3$ and $d_{14} = -0.693$ pm/V. In the KDP [72], measured coefficients are $d_{14} = d_{25} = 1.3$ pm/V, $d_{36} = 21$ pm/V.

Typically, piezoelectric materials are compared by their electromechanical properties, therefore electromechanical coupling constants are introduced in [73], which are defined in tensor notation as $k_{ij} = \sqrt{d_{ij}^2/(S_{jj}^E \varepsilon_0 \varepsilon_{ii}^\sigma)}$, $\varepsilon_{ij}$ being dielectric constant. This dimensionless coefficient can be determined for all piezoelectric materials and represents the ratio between the electrical energy output and the mechanical energy input. For PZT, which is the most commonly used in energy harvesting applications [69] $k_{31} = 0.44$, for LiNbO$_3$ it is 0.49, for ZnO it is 0.19. For the studied phosphates, the electromechanical coupling constants are given in Table 7.

Low values of the piezotensor components also lead to low values of the electromechanical coupling constants. Thus, for $k_{31}$, in the case of KZPO, RZPO they are approximately 100 times less than in PZT. Only $k_{14}, k_{15}$ coefficients have values in KSPO comparable to those in ZnO. Thus, the phosphates under study, in contrast to GaPO$_4$ [70,65], are not of interest for use as piezoelectric materials.

## 5. Linear and nonlinear optical properties

Linear and nonlinear optical properties of NLO materials have been widely studied [74]. Infrared spectroscopy is a valuable analytical technique and is used to study the structure of NLO materials. Infrared absorption spectra (IRS) of cyclophosphates were measured for KZPO, RZPO in [26], and for KMPO, RCPO in [22] and for KSPO in [16]. It is known that IRS of phosphates are characterized by a set of peaks in the region of $1280-1070$ cm$^{-1}$, which arise due to asymmetric stretching vibrations of O−P−O. Peaks around $980-715$ cm$^{-1}$ are assigned to the symmetric stretching vibration of O−P−O, and bands in the region of $\sim 900$ cm$^{-1}$ are assigned to asymmetric stretching vibrations of P−O−P, whereas the $760-680$ cm$^{-1}$ bands are assigned to the symmetric stretching vibration of P−O−P. The main frequency group of [P$_3$O$_9$] is within the interval of $600-400$ cm$^{-1}$ ($\delta$(O−P−O)).

To select the optimal calculation model, gradient PBE-D3, PBEsol, hybrid PBEsol0, B3LYP and LC-wPBEsol functionals were used. The application of these functionals to the calculation of the vibrational frequencies of KZPO yields the root-mean-square deviation from the data of [24] in the following sequence: 8.6, 6.9, 2.4, 4.6, and 6.3%. At the same time, gradient functionals underestimate the frequencies, and hybrid functionals, on the contrary, overestimate them. The PBEsol0 functional shows optimal results compared to the experiment. Similar data with the PBE-D3, PBEsol, PBEsol0, LC-wPBEsol functionals were obtained for RZPO: 7.8, 6.6, 2.7, 7.1%. A comparative analysis for the KMPO showed a slightly better result for the PBEsol functional.
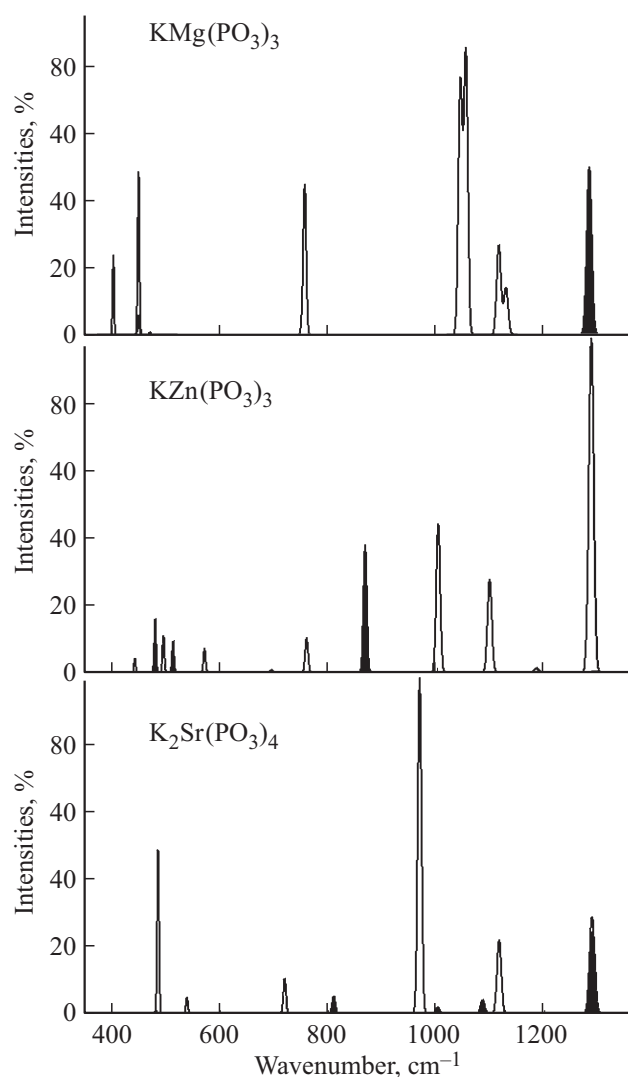
**Figure 5.** Dependences of the intensities of spectra (%) of infrared absorption on wave numbers (cm$^{-1}$) of cyclophosphates.

In the following, the results are presented for the calculation of IRS with the hybrid PBEsol0 functional.

Figure 5 shows the infrared absorption spectra in the interval of $400-1400$ cm$^{-1}$ obtained by Gaussian broadening of the frequencies of normal long-wave ($\mathbf{k} = 0$) oscillations for KMPO, KZPO KSPO. For convenience of comparison, the intensities are given in %, and the maximum values are 3755, 2397, 3392 km/mol, respectively. The complete vibrational representation, by which the atomic displacement vectors are transformed, is divided into irreducible representations. For IRS of KMPO these will be singly degenerate $A_2''$ and doubly degenerate $E'$ with $\mathbf{E} \parallel \mathbf{z}$ and $\mathbf{E} \perp \mathbf{z}$ polarization of the light. The $c$ axis is chosen as the direction of $\mathbf{z}$ everywhere. In the KZPO, the corresponding representations are $A, E$, and in the KSPO they are $B, E$. In Figure 5, vibrations with the polarization along $\mathbf{z}$ correspond to bands highlighted in black. For the KCPO, RCPO the spectra are similar those of the KMPO,

and for the RZPO they are similar to those of the KZPO. Wave numbers $\nu$ of the vibrations active in the IRS are given in Table 8, where the polarization is specified in parentheses.

In the KCPO (KMPO, RCPO), modes of the $A_2''$ symmetry are built due to vibrations of Ca, K, P, O2 atoms in the direction of $z$ and O1 in $xyz$. For a mode with a wavenumber of 1270.2 cm$^{-1}$, the Ca, K, O2, O1, and P atoms are displaced in opposite directions of $z$. The contribution to the total amplitude of vibrations for Ca, K, O2 atoms is insignificant, whereas the contribution from P is equal to 21.7%, and that from O1 is 78.3%. Thus, this is a typical O1$-$P$-$O1 vibration. For a wave number of 530.7 cm$^{-1}$, the Ca, K, O2, and P, O1 atoms are displaced in opposite directions with amplitudes of 17.0.28 and 7.47%, respectively. In this case the atoms in the CaO1$_6$ octahedron and in the [P$_3$O$_9$] anion vibrate.

Degenerate modes with $E'$ symmetry correspond to vibrations of Ca, K atoms in opposite directions of $x(y)$, P, O2 — in $xy$ plane, and O1 — in $xyz$. For a mode with a wavenumber of 1054.3 cm$^{-1}$, the contribution of phosphorus atoms is 3%, whereas that of O2 is 96%. The P and O2 atoms are displaced in opposite directions, which corresponds to the declared symmetrical $\nu$(O2$-$P$-$O2) type. For a mode with a wavenumber of 756.8 cm$^{-1}$, the contribution of P is 11%, that the contribution of O2 is 84%, and that of O1 is 5% and for a wavenumber of 449.3 cm$^{-1}$, they are 6, 79, 15%, respectively. These vibrations correspond to the symmetrical type $\nu$(P$-$O2$-$P) and $\delta$(O$-$P$-$) types.

In the crystals of KZPO, RZPO with $R3$ symmetry, the atomic displacement vectors related to the irreducible representation $A$ are built up from vibrations of metal and fluorine atoms in opposite directions along the $z$ axis. The latter also vibrate in the $xy$-plane. Nonequivalent oxygen atoms O1, O2, O3 are displaced in $xyz$-directions. Thus, for a wave number of 875.3 cm$^{-1}$, the contribution of P atoms is 8%, and the contribution of O3 atoms is 89%. Due to the fact that [P$_3$O$_9$] rings are formed in the $xy$ plane by means of O3 atoms, this type of vibrations refers to asymmetric $\nu$(O3$-$P$-$O3). For vibrations with a wave number of 519.1 cm$^{-1}$, the percentage of fluorine increased to 21%, and those of the oxygen atoms O1, O2, and O3 increased to 14, 45, and 20%, respectively. Thus, it is $\delta$(O$-$P$-$O)-type.

For the $xy$ polarization of the irreducible representation $E$, metal atoms vibrate only in a plane, and fluorine and oxygen atoms vibrate in three dimensions. In the case of a mode with a wave number of 1275.1 cm$^{-1}$, fluorine atoms with an amplitude of 28% are displaced in the opposite direction to the O1 (26%), O2 (45%) atoms, which represents asymmetric oscillations of O1$-$P$-$O2. In contrast to this, a mode with a wave number of 1004.1 cm$^{-1}$ corresponds to vibrations of O3$-$P$-$O3 with a fluorine percentage of 19% and that of oxygen O3 equal to 78%.

The polarization vectors of vibrational modes of K$_2$Sr(PO$_3$)$_4$ confirm the already established patterns.

**Table 8.** Wave numbers $\nu$ (cm$^{-1}$) of normal long-wave vibrations active in the infrared spectra, with the polarization dependence and intensity ranges specified from very low to very high: $\nu^{vl} < 50$ km/mol — $\nu^{l} < 500$ km/mol — $\nu^{m} < 1000$ km/mol — $\nu^{b} < 2000$ — $\nu^{vb}$

| KMg(PO$_3$)$_3$ | KCa(PO$_3$)$_3$ | RbCd(PO$_3$)$_3$ | KZn(PO$_3$)$_3$ | RbZn(PO$_3$)$_3$ | K$_2$Sr(PO$_3$)$_4$ |
|---|---|---|---|---|---|
| $402.9^m(xy)$ | | | $448.4^l(xy)$ | $440.8^l$ | $401.2^{vl}(xy)$ |
| $449.3^m(z)$ | | | $480.5^m(z)$ | $478.2^m$ | $481.1^{vl}(z)$ |
| $449.3^b(xy)$ | $460.7^b$ | $452.8^b$ | $493.4^l(xy)$ | $493.7^l$ | $485.2^b(xy)$ |
| $470.0^{vl}(xy)$ | $468.1^{vl}$ | $456.4^l$ | $519.1^m(z)$ | $511.6^l$ | $539.1^l(xy)$ |
| $530.6^{vl}(z)$ | $528.3^{vl}$ | $580.7^l$ | $568.5^l(xy)$ | $569.6^l$ | $576.2^{vl}(z)$ |
| $756.8^b(xy)$ | $757.7^b$ | $751.3^b$ | $698.4^{vl}(z)$ | $692.4^l$ | $719.5^l(xy)$ |
| $752.8^l(xy)$ | $755.3^{vl}$ | $748.2^l$ | $768.0^l(xy)$ | $758.5^l$ | $810.2^l(z)$ |
| $1044.0^{vb}(xy)$ | $1054.3^{vb}$ | $1032.6^{vb}$ | $875.3^b(z)$ | $866.7^b$ | $969.3^{vb}(xy)$ |
| $1054.3^{vb}(xy)$ | $1057.8^{vb}$ | $1040.7^{vb}$ | $1004.1^b(xy)$ | $1001.7^b$ | $1002.1^l(z)$ |
| $1115.5^b(xy)$ | $1106.1^b$ | $1097.8^m$ | $1092.6^m(xy)$ | $1096.9^m$ | $1085.5^l(z)$ |
| $1128.7^m(xy)$ | $1111.3^l$ | $1108.9^m$ | $1175.9^l(z)$ | $1182.5^{vl}$ | $1116.2^m(xy)$ |
| $1282.4^{vb}(z)$ | $1270.2^{vb}$ | $1273.5^{vb}$ | $1275.1^{vb}(xy)$ | $1284.4^{vb}$ | $1287.7^b(xy)$ |
| | | | $1282.5^{vl}(z)$ | $1288.8^l$ | $1288.8^b(z)$ |

For singly degenerate modes with $B$ symmetry with $z$-polarization for a wave number of 1288.8 cm$^{-1}$ O1−P−O2 atoms oscillate with amplitude contributions of $45\%−17\%−38\%$, and for symmetric O1−P−O2 the contributions are $38\%−14\%−46\%$. For modes with $E$ symmetry with $xy$-polarization for $\nu$(O1−P−O2) with a wave number of 1287.7 cm$^{-1}$ the contributions of atoms are $36\%−30\%−34\%$, and for $\nu$(P−O3−P) with 969.3 cm$^{-1}$ the contribution of phosphorus is 10%, and that of oxygen is 89%.

To assess the nonlinear optical properties of phosphates, the SHG coefficients $g_{ij}$ were used, which were calculated using the CKPS procedure [44,46] in a.u. from the first hyperpolarizability $\beta$, third-order electrical susceptibility tensor $\chi^{(2)}$:

$$g_{ij} = \frac{1}{2}\chi^{(2)} = \frac{\pi}{V}\beta_{ij}$$

(in Voigt notation). To select the optimal calculation model, the experimental data for the model KDP were used. It has a set of properties such as piezoelectric, ferroelectric, electro-optical, nonlinear optical, which are used in various applications. This is the first material that, thanks to its nonlinear properties, opened a promising era in the field of photonics [75]. The crystal structure of KDP was studied in [76], and it was shown that under ordinary conditions it belongs to a tetragonal system with symmetry space group $I\bar{4}2d$ (N 122). Its experimental studies were carried out in [77,78], and theoretical studies were published in [79,67].

NLO properties of the KDP were calculated *ab initio* with various functionals, and the results for some of them are given in Table 9.

It can be seen that the gradient functionals PBE and PBESOL overestimate the SHG $g_{36}$ coefficient, whereas the hybrid PBE0 and PBESOL0 functionals underestimate it. For $\Delta n$ birefringence the situation is the opposite. The experimental value of $g_{36}$ is obtained by calculating

**Table 9.** Experimental (Exp.[Ref]) and calculated parameters of the $a, c, V$ structure and NLO properties ($g_{ij}, \Delta n$) of the KDP

| Method | $a$, Å | $c$, Å | $V$, Å$^3$ | $g_{36}$, pm/V | $\Delta n$ |
|---|---|---|---|---|---|
| Exp. [77,78] | 7.456 [77] | 6.975 | 387.20 | 0.39 [78] | |
| Theor. [79] | 7.453 [79] | 6.971 | | | 0.064 [79] |
| PBE | 7.533 | 6.976 | 395.82 | 0.460 | 0.070 |
| PBE0 | 7.464 | 6.922 | 385.67 | 0.335 | 0.062 |
| PBEsol | 7.432 | 6.847 | 378.16 | 0.461 | 0.069 |
| PBEsol0 | 7.388 | 6.824 | 372.47 | 0.338 | 0.061 |

**Table 10.** SHG $g_{ij}$ coefficients (pm/V) and $\Delta n$ birefringence index for cyclophosphates

| Crystal | $g_{11}$ | $g_{15}$ | $g_{16}(g_{14})$ | $g_{33}$ | $-\Delta n$ |
|---|---|---|---|---|---|
| KCa(PO$_3$)$_3$ | −0.034 | | | | 0.001 |
| KMg(PO$_3$)$_3$ | −0.211 | | | | 0.007 |
| RbCd(PO$_3$)$_3$ | −0.029 | | | | 0.015 |
| KZn(PO$_3$)$_3$ | −0.260 | 0.385 | 0.422 | −0.616 | 0.005 |
| RbZn(PO$_3$)$_3$ | −0.197 | 0.356 | 0.453 | −0.434 | 0.001 |
| K$_2$Sr(PO$_3$)$_4$ | | 0.251 | (−0.107) | | 0.022 |

the average value between the corresponding gradient and hybrid functionals.

Table 10 shows the SHG $g_{ij}$ coefficients (pm/V) and $\Delta n$ birefringence calculated with the PBEsol functional for cyclophosphates.

Due to the symmetry for hexagonal crystals $g_{xxx} \equiv g_{11} = -g_{12} \equiv g_{xyy}$, for trigonal crystals $g_{12} = -g_{11}$, $g_{22} = -g_{16}$, $g_{24} = g_{15}$, and in the tetragonal crystal $g_{24} = -g_{15}$. In the hexagonal KMPO, KCPO, RCPO, only one component of the tensor is nonzero: $g_{11}$. In relation to the $g_{36}$ of KDP, the SHG efficiency indicator will be 0.5, 0.1, 0.1, respectively. For the RCPO this is consistent with the experimental data [22]. At the same time, for

the KMPO it is twice higher than the value determined in [22]. The lower SHG efficiency may also be indicated by the low birefringence $\Delta n$ — two times less than in the RCPO. The symmetry of the space group $R3$ in $AZn(PO_3)_3$ ($A = K, Rb$) determines four non-zero independent SHG coefficients ($g_{11}$, $g_{15}$, $g_{16}$ and $g_{33}$). The values of $g_{11}$, $g_{15}$, $g_{33}$ coefficients calculated in [24] for the KZPO, RZPO are less than those shown in Table 10, and value of $g_{16}$ is greater than in the table. When comparing experimental and theoretical SHG coefficients, it should be kept in mind that in the first case the incident light has a finite wavelength (usually 1064 nm), and in the second case it is assumed to be infinite.

To evaluate the efficiency of SHG, the effective coefficient $g_{\text{eff}}$ was obtained by averaging the values from Table 10, and then the efficiency itself was calculated. For the KZPO this yielded a value of 0.6 KDP, which coincides with the experimental one, and for the RZPO it yielded only 0.5, which is less than in the KZPO and in the experiment [26]. For the tetragonal KSPO, averaging the coefficients gives a theoretical efficiency of 0.4 KDP. Similar data for the PBEsol0 functional results in significantly lower values. For all the studied phosphates, very low birefringence values were obtained, which is generally non-typical for NLO crystals.

The studied phosphates, in contrast to double carbonates [49], belong to non-centrosymmetric crystals with non-zero $g_{ij}$ coefficients. However, another important birefringence index for NLO materials turned out to be orders of magnitude lower than in double carbonates with a planar anion, where it is approximately 0.16. Apparently, low birefringence is a distinctive property of cyclophosphates.

## 6. Conclusion

*Ab ininio* studies show that in KMg(PO$_3$)$_3$, KCa(PO$_3$)$_3$, RbCd(PO$_3$)$_3$ layered hexagonal phosphates fluorine and oxygen atoms form [P$_3$O$_9$], which are combined into infinite Z-shaped chains in the direction of $c$ axis. In the trigonal KZn(PO$_3$)$_3$, RbZn(PO$_3$)$_3$) bound structures are formed in the form of trimers [P$_3$O$_9$], united through zinc atoms into hexagonal rings around K(Rb) atoms. In the K$_2$Sr(PO$_3$)$_4$ four anions form a [P$_4$O$_{12}$] ring, and the electron clouds of these rings weakly overlap in the direction of $c$ axis. The obtained infrared absorption spectra are confirmed by the available experimental data and indicate the presence of complex anionic structural formations in phosphates.

From calculations of the band structure and the total and partial density of states, it follows that the width of the indirect band gap between the upper valence bands formed by the $p$-states of oxygen atoms O1 and the lower unoccupied $p$-band of phosphorus states is 5.98, 6.29, 5.60 eV in hexagonal, 6.4 eV in trigonal and 6.9 eV in tetragonal K$_2$Sr(PO$_3$)$_4$. The calculated second harmonic generation coefficients for $AZn(PO_3)_3$ ($A = K, Rb$), KCa(PO$_3$)$_3$ turned out to be 0.6, 0.5, and 0.1 times higher than in the KDP.

This suggests that the studied phosphates may be promising for use as nonlinear optical materials in the deep ultraviolet region.

From calculations of elastic constants, linear uniaxial compression moduli were obtained, which indicate weak elastic anisotropy, and the ratio of the bulk compression modulus to the shear modulus indicates plasticity of KCa(PO$_3$)$_3$, RbCd(PO$_3$)$_3$. These same compounds have a lower Debye temperature and a minimum thermal conductivity coefficient. The obtained direct and inverse piezotensor constants have low values, and therefore the non-centrosymmetric cyclophosphates under study are unlikely to have practical applications.

### Conflict of interest

The author declares that he has no conflict of interest.

## References

[1] C. Wu, G. Yang, M.G. Humphrey, C. Zhang. Coordinat. Chem. Rev. **375**, 459 (2018). https://doi.org/10.1016/j.ccr.2018.02.017

[2] Y. Liu, Y. Shen, S. Zhao, J. Luo. Coordinat. Chem. Rev. **407**, 213152 (2020). https://doi.org/10.1016/j.ccr.2019.213152

[3] R.A. Kumar. J. Chem. **2013**, 154862 (2013). https://doi.org/10.1155/2013/154862

[4] D.A. Roberts. IEEE J. Quantum Electron. **28**, *10*, 2057 (1992). https://ieeexplore.ieee.org/document/159516

[5] B.I. Kidyarov. Crystals **7**, *4*, 109 (2017). https://doi.org/10.3390/cryst7040109

[6] T. Thao Tran, H. Yu, J.M. Rondlinelli, K.R. Poeppelmeier, P.S. Halasyamani. Chem. Mater. **28**, *15*, 5238 (2016). https://doi.org/10.1021/acs.chemmater.6b02366

[7] W. Wang, D. Mei, S. Wen, J. Wang, Y. Wu. Chin. Chem. Lett. **33**, *5*, 2301 (2022). https://doi.org/10.1016/j.cclet.2021.11.089

[8] I.V. Nikiforov, D.V. Deyneko, I.F. Duskaev. Phys. Solid State **62**, *5*, 860 (2020).

[9] M. Mutailipu, K.R. Poeppelmeier, S. Pan. Chem. Rev. **121**, *3*, 1130 (2021). https://doi.org/10.1021/acs.chemrev.0c00796

[10] Q. Jing, G. Yang, J. Hou, M. Sun, H. Cao. J. Solid State Chem. **244**, 69 (2016). https://doi.org/10.1016/j.jssc.2016.08.036

[11] X. Liu, P. Gong, Y. Yang, G. Song, Z. Lin. Coordinat. Chem. Rev. **400**, 213045 (2019). https://doi.org/10.1016/j.ccr.2019.213045

[12] Y.-X. Song, L. Min, Y. Ning. Chinese J. Struct. Chem. **39**, *12*, 2148 (2020). DOI: 10.14102/j.cnki.0254-5861.2011-3028

[13] J. Dang, D. Mei, Y. Wu, Z. Lin. Coordinat. Chem. Rev. **431**, 213692 (2021). https://doi.org/10.1016/j.ccr.2020.213692

[14] Z. Bai, L. Liu, D. Wang, C.-L. Hu, Z. Lin. Chem. Sci. **12**, *11*, 4014 (2021). DOI: 10.1039/d1sc00080b

[15] S.G. Zhao, P.F. Gong, S.Y. Luo, L. Bai, Z.S. Lin, C.M. Ji, T.L. Chen, M.C. Hong, J.H. Luo. J. Am. Chem. Soc. **136**, *24*, 8560 (2014). https://doi.org/10.1021/ja504319x

[16] Z. Bai, L. Liu, L. Zhang, Y. Huang, F. Yuan, Z. Lin. Chem. Commun. **55**, *58*, 8454 (2019). DOI: 10.1039/c9cc04192c

[17] L. Li, Y. Wang, B.H. Lei, S.J. Han, Z.H. Yang, P.K. Roeppelmeier, S.L. Pan. J. Am. Chem. Soc. **138**, *29*, 9101 (2016). https://doi.org/10.1021/jacs.6b06053

[18] L. Li, Y. Wang, B.-H. Lei, S. Han, Z. Yang, H. Li, S. Pan. J. Mater. Chem. C **5**, *2*, 269 (2017). DOI: 10.1039/c6tc04565k

[19] M. Wen, H.P. Wu, S.C. Cheng, J. Sun, Z.H. Yang, X.H. Wu, S.L. Pan. Inorg. Chem. Front. **6**, *2*, 504 (2019).

[20] N.E. Novikova, N.I. Sorokina, I.A. Verin, O.A. Alekseeva, E.I. Orlova, V.I. Voronkova, M. Tseitlin. Crystals **8**, *7*, 283 (2018). https://doi.org/10.3390/cryst8070283

[21] P. Yu, L.-M. Wu, L.-J. Zhou, L. Chen. J. Am. Chem. Soc. **136**, *1*, 480 (2014).

[22] M. Abudoureheman, X. Pan, S. Han, Y. Rouzhahong, Z. Yang, H. Wu, S. Pan. Inorg. Chem. **57**, *12*, 7372 (2018). https://doi.org/10.1021/acs.inorgchem.8b01017

[23] Z. Xie, X. Su, H. Ding, H. Li. J. Solid State Chem. **262**, 313 (2018). https://doi.org/10.1016/j.jssc.2018.03.032

[24] T. Yu, L. Xiong, X. Liu, Y. Yang, Z. Lin, L. Wu, L. Chen. Cryst. Growth Design **21**, *4*, 2445 (2021). https://doi.org/10.1021/acs.cgd.1c00051

[25] M. Sandstrom, D. Bostrom. Acta Crystallographica E **60**, *Part 2*, i15 (2004). DOI: https://doi.org/10.1107/S1600536804000303

[26] S. Wang, C. Xu, X. Qiao. Opt. Mater. **107**, 110102 (2020). https://doi.org/10.1016/j.optmat.2020.110102

[27] D. Wei, H.J. Seo. J. Lumin. **229**, 117644 (2021). https://doi.org/10.1016/j.jlumin.2020.117644

[28] R. Dovesi, A. Erba, R. Orlando, C.M. Zicovich-Wilson, B. Civalleri, L. Maschio, M. Rérat, S. Casassa, J. Baima, S. Salustro, B. Kirtman. WIREs Comput. Mol. Sci. **8**, *4*, e1360 (2018). https://doi.org/10.1002/wcms.1360

[29] D. Vilela Oliveira, J. Laun, M.F. Peintinger, T. Bredow. J. Comput. Chem. **40**, *27*, 2364 (2019). https://doi.org/10.1002/jcc.26013

[30] J. Laun, D. Vilela Oliveira, T. Bredow. J. Comput. Chem. **39**, *19*, 1285 (2018). https://doi.org/10.1002/jcc.25195

[31] J.P. Perdew, K. Burke, M. Ernzerhof. Phys. Rev. Lett. **77**, *18*, 3865 (1996). https://doi.org/10.1103/PhysRevLett.77.3865

[32] J.P. Perdew, A. Ruzsinszky, G.I. Csonka, O.A. Vydrov, G.E. Scuseria, L.A. Constantin, X. Zhou, K. Burke. Phys. Rev. Lett. **100**, *13*, 136406 (2008); Erratum Phys. Rev. Lett. **102**, 039902 (2009). https://doi.org/10.1103/PhysRevLett.100.136406

[33] A.D. Becke. J. Chem. Phys. **98**, *7*, 5648 (1993). https://doi.org/10.1063/1.464913

[34] C. Lee, W. Yang, R.G. Parr. Phys. Rev. B **37**, *2*, 785 (1988). https://doi.org/10.1103/PhysRevB.37.785

[35] C. Adamo, V. Barone. J. Chem. Phys. **110**, *13*, 6158 (1999). https://doi.org/10.1063/1.478522

[36] A.V. Krukau, O.A. Vydrov, A.F. Izmaylov, G.E. Scuseria. J. Chem. Phys. **125**, *22*, 224106 (2006). https://doi.org/10.1063/1.2404663

[37] L. Schimka, J. Harl, G. Kresse. J. Chem. Phys. **134**, *2*, 024116 (2011). https://doi.org/10.1063/1.3524336

[38] E. Weintraub, T.M. Henderson, G.E. Scuseria. J. Chem. Theory Comput. **5**, *4*, 754 (2009). https://doi.org/10.1021/ct800530u

[39] N. Handy, T. Yanai, D. Tew. Chem. Phys. Lett. **393**, *1−3*, 51 (2004). https://doi.org/10.1016/j.cplett.2004.06.011

[40] R. Menchón, G. Colizzi, C. Johnston, F. Torresi, J. Lasave, S. Koval, J. Kohanoff, R. Migoni. Phys. Rev. B **98**, *10*, 104108 (2018). https://doi.org/10.1103/PhysRevB.98.104108

[41] D.C. Langreth, M. Dion, H. Rydberg, E. Schröder, P. Hyldgaard, B.I. Lundqvist. Int. J. Quantum Chem. **101**, *5*, 599 (2005). https://doi.org/10.1002/qua.20315

[42] S. Grimme, A. Hansen, J.G. Brandenburg, C. Bannwarth. Chem. Rev. **116**, *9*, 5105 (2016). https://doi.org/10.1002/jcc.21759

[43] S. Grimme, S. Ehrlich, L. Goerigk. J. Comput. Chem. **32**, *7*, 1456 (2011). https://doi.org/10.1002/jcc.21759

[44] M. Ferrero, M. Rérat, R. Orlando, R. Dovesi. J. Chem. Phys. **128**, *1*, 014110 (2008). https://doi.org/10.1063/1.2817596

[45] R. Orlando, V. Lacivita, R. Bast, K. Ruud. J. Chem. Phys. **132**, *24*, 244106 (2010). https://doi.org/10.1063/1.3447387

[46] M. Ferrero, M. Rérat, B. Kirtman, R. Dovesi. J. Chem. Phys. **129**, *24*, 244110 (2008). https://doi.org/10.1063/1.3043366

[47] M. Ferrero, B. Civalleri, M. Rérat, R. Orlando, R. Dovesi. J. Chem. Phys. **131**, *21*, 214704 (2009). https://doi.org/10.1063/1.3267861

[48] H.J. Monkhorst, J.D. Pack. Phys. Rev. B **13**, *12*, 5188 (1976).

[49] Yu.N. Zhuravlev. Phys. Solid State **64**, *11*, 1700 (2022).

[50] J. Sun, H. Wu, M. Mutailipu, Z. Yang, S. Pan. Dalton Trans. **48**, *35*, 13406 (2019). https://doi.org/10.1039/C9DT02842K

[51] Yu.N. Zhuravlev, D.V. Korabel'nikov. Bull. Russ. Academ. Sci. **86**, *10*, 1230 (2022).

[52] W.F. Perger, J. Criswell, B. Civalleri, R. Dovesi. Comp. Phys. Commun. **180**, *10*, 1753 (2009). https://doi.org/10.1016/j.cpc.2009.04.022

[53] A. Erba, A. Mahmoud, R. Orlando, R. Dovesi. Phys. Chem. Minerals **41**, *2*, 151 (2014). https://doi.org/10.1007/s00269-013-0630-4

[54] Z. Hu, M. Lan, D. Huang, P. Huang, S. Wang. Crystals **12**, *9*, 1323 (2022). https://doi.org/10.3390/ cryst12091323

[55] M. Born, K. Huang. Dynamics Theory of Crystal Lattices. Oxford University Press, Oxford, UK (1954).

[56] F. Mouhat, F.-X. Coudert. Phys. Rev. B **90**, *22*, 224104 (2014). https://doi.org/10.1103/PhysRevB.90.224104

[57] N.A. Abdullaev. Phys. Solid State **48**, *4*, 663 (2006).

[58] P. Jund, R. Viennois, X.M. Tao, K. Niedziolka, J.C. Tedenac. Phys. Rev. B **85**, *22*, 224105 (2012). https://doi.org/10.1103/PhysRevB.85.224105

[59] W. Voigt. Lehrbuch der Kristallphysik. Teubner, Leipzig (1928). https://doi.org/10.1007/978-3-663-15884-4

[60] A. Reuss. Z. Angew. Math. Mech. **9**, *1*, 4958 (1929). https://doi.org/10.1002/zamm.19290090104

[61] R. Hill. J. Mechan. Phys. Solids **11**, *5*, 357 (1963). https://doi.org/10.1016/0022-5096(63)90036-X

[62] Yu.N. Zhuravlev, Izv. AltGU, Fizika **1**, *123*, 23 (2022) (in Russian). https://doi.org/10.14258/izvasu(2022)1-03

[63] Y. Zhuravlev, V. Atuchin. Molecules **27**, *20*, 6840 (2022). https://doi.org/10.3390/molecules27206840

[64] S.F. Pugh. The London, Edinburgh, and Dublin Philos. Mag. J. Sci. **45**, *367*, 823 (1954).

[65] Y. Zhou, B. Liu. J. Eur. Ceram. Soc. **33**, *13−14*, 2817 (2013). http://dx.doi.org/10.1016/j.jeurceramsoc.2013.04.020

[66] O.L. Anderson. J. Phys. Chem. Solids **24**, *7*, 909 (1963). https://doi.org/10.1016/0022-3697(63)90067-2

[67] R.E. Menchón, F. Torresi, J. Lasave, S. Koval. Condens. Matter Phys. **25**, *4*, 43709 (2022). https://doi.org/10.48550/arXiv.2301.01538

[68] D.R. Clarke. Surf. Coat. Technol. **163−164**, 67 (2003). https://doi.org/10.1016/S0257-8972(02)00593-5

[69] A. Erba, Kh.E. El-Kelany, M. Ferrero, I. Baraille, M. Rerat. Phys. Rev. B **88**, *3*, 035102 (2013). DOI: 10.1103/PhysRevB.88.035102

[70] P. Krempl, G. Schleinzer, W. Wallnöfer. Sensors. Actuators A **61**, *1−3*, 361 (1997). https://doi.org/10.1016/S0924-4247(97)80289-0

[71] C.R. Bowen, V.Y. Topolov, A.K. Hyunsun. Modern Piezo-electric Energy-Harvesting Materials (Springer Series in Materials Science, 238). Springer Int. Publishing, Imprit, Springer (2016).

[72] E.J.L. Gomes, S.G.C. Moreira, A.S. de Menezes, A.O. dos Santos, D.P. Pereira, P.C. de Oliveira, C.M.R. Remédios. J. Synchrotron Rad. **17**, *Part 6*, 810 (2010). https://doi.org/10.1107/S0909049510039956

[73] G. Clementi, F. Cottone, A. Di Michele, L. Gammaitoni, M. Mattarelli, G. Perna, M. López-Suárez, S. Baglio, C. Trigona, I. Neri. Energies **15**, *17*, 6227 (2022). https:// doi.org/10.3390/en15176227

[74] Y. Wang, D. Sun, J. Chen, C. Shen, G. Liu, D. Wang, S. Wang. Optik **251**, 168481 (2022). https://doi.org/10.1016/j.ijleo.2021.168481

[75] P. Santhanaraghavan, P. Ramasamy. Sci. Technol. **2**, 53 (2001). DOI: 10.1016/B0-08-043152-6/00010-3

[76] G.M. Meyer, R.J. Nelmes, C. Vettier. J. Phys. C **13**, *21*, 4035 (1980). https://iopscience.iop.org/article/10.1088/0022-3719/13/21/009

[77] K. Manimekalai, P. Jayaprakash, N. Padmamalini, S. Rama. J. Mater. Sci.: Mater. Electron. **34**, 171 (2023). https://doi.org/10.1007/s10854-022-09594-8

[78] P.S. Halasyamani, W. Zhang. Inorg. Chem. **56**, *3*, 12077 (2017). DOI: 10.1021/acs.inorgchem.7b02184

[79] H.A.R. Aliabad, M. Fathabadi, I. Ahmad. Int. J. Quantum Chem. **113**, *6*, 865 (2012). https://doi.org/10.1002/qua.24258

*Translated by Y.Alekseev*